Targeting Fibrotic Scars with Extracellular Vesicles Extracted from Mature Aloe vera: Enhanced Antioxidant, Anti-inflammatory, and Antifibrotic Activity through M2 Macrophage Polarization and Myofibroblasts Inhibition

*M. Camila Ceballos-Santa [1,2], Tom Gaborski [2], Karin Wuertz-Kozak [2,3]**

[1] Department of Industrial and Systems Engineering, Rochester Institute of Technology, Rochester, NY 14632, USA

[2] Department of Biomedical Engineering, Rochester Institute of Technology, Rochester, NY 14632, USA

[3] Schön Clinic Munich Harlaching, Spine Center, Academic Teaching Hospital and Spine Research Institute of the Paracelsus Medical University Salzburg (Austria), 81547 Munich, Germany

*Corresponding author: kwbme@rit.edu

Abstract

Background: Abnormal scarring and fibrotic skin disorders arise from dysregulated wound healing processes. While Aloe vera is widely recognized for its therapeutic properties, the potential of its extracellular vesicles (Av-EVs) remains underexplored.

Objective: This study aimed to isolate and characterize Av-EVs and evaluate their antioxidant, anti-inflammatory, and antifibrotic properties *in vitro*, focusing on the impact of extraction method and plant maturity.

Methods: Av-EVs were isolated from mature Aloe vera leaves using manual (NB) or blender-based (B) homogenization. Vesicles were characterized by nanoparticle tracking analysis, transmission electron microscopy, and protein quantification. Antioxidant and cytotoxicity assays (DPPH, alamarBlue) were followed by functional anti-inflammatory and antifibrotic analyses respectively in LPS-stimulated THP-1 macrophages and TGF-β1/Vitamin C-activated human dermal fibroblasts (RT-qPCR, immunofluorescence).

Results: NB-derived EVs from mature leaves exhibited the most potent activity across all assays, showing superior antioxidant capacity, greater suppression of pro-inflammatory cytokines, enhanced M2/M2a macrophage polarization, and significant downregulation of COL1A1 and α-SMA. In contrast, B-derived and young leaf-derived EVs showed reduced bioactivity, with young EVs failing to inhibit fibrotic markers.

Conclusion: Manually extracted Av-EVs from mature leaves demonstrate superior multifunctional bioactivity, highlighting their potential as plant-derived nanotherapeutics for fibrotic scar modulation.

Keywords
Wound healing, oxidative stress, inflammation resolution, myofibroblast differentiation, regenerative skin therapy

1. Introduction

Disruptions in the tightly regulated wound healing process – hemostasis, inflammation, proliferation, and remodeling – can lead to pathological outcomes, ranging from chronic nonhealing wounds to excessive fibrotic scarring. The latter is characterized by aberrant collagen accumulation, disorganized extracellular matrix (ECM) remodeling, and persistent myofibroblast activation driven by abnormal fibroblast proliferation and transdifferentiation.[1] Among the principal causes of abnormal wound healing are chronic inflammation and oxidative stress, which induce intracellular overproduction of reactive oxygen species (ROS).[2] Excess ROS not only damage cellular macromolecules such as lipids, proteins, and DNA, but also perpetuate pro-inflammatory signaling and impair tissue regeneration.[3] In this dysregulated microenvironment, ROS activate latent transforming growth factor-beta (TGF-β), which in turn promotes fibroblast-to-myofibroblast differentiation and excessive secretion of collagen and α-smooth muscle actin (α-SMA) – a critical protein for wound contraction. These molecular events ultimately result in the formation of fibrotic scar tissue, clinically recognized as hypertrophic scars and keloids.[4, 5]

To mitigate such outcomes, Aloe vera has been extensively studied for its diverse pharmacological properties and high concentration of bioactive constituents.[6-8] This succulent plant harbors over 200 compounds and 75 nutrients, including soluble sugars, lipids, proteins, polysaccharides and lignin, polyphenols, enzymes, vitamins (e.g., A, C, E, B_1, B_2, B_{12}) and minerals (e.g., calcium, potassium, sodium, magnesium),[9] which collectively confer its wound healing, anti-inflammatory, antioxidant, antimicrobial, immunomodulatory, analgesic, and moisturizing benefits.[10, 11]

Historically, Aloe vera research has centered on topical and oral formulations. A large body of evidence, including *in vitro* studies, preclinical models, and human clinical trials, has consistently demonstrated the therapeutic efficacy of Aloe vera-based products.[12-29] However, a promising new frontier in this research has emerged with the exploration of plant-derived extracellular vesicles (PDEVs) – nanoscale membranous particles secreted by plant cells that not only retain the therapeutic attributes of their source tissue but also offer target delivery capabilities. By delivering a diverse cargo of lipids, nucleic acids, proteins, metabolites, and even pharmacological compounds, PDEVs can mediate intracellular and intercellular communication, maintain tissue homeostasis, and support regenerative processes.[30]

Compared to their mammalian counterparts, PDEVs offer multiple advantages beyond their typical mechanism of action, such as being ethically uncontroversial, cost-effective and scalable, and evidence thus far suggests that they do not pose risk of carcinogenesis, immunogenicity, or tissue rejection. Additionally, they overcome key limitations of synthetic and mammalian EV-based drug delivery systems, including low yield, short bioavailability, poor loading efficiency, and limited tissue targeting.[30-34] For these reasons, PDEVs are now considered as a new class of cell-free therapeutic platforms with high potential for clinical translation and preventive healthcare.

Among PDEVs, Aloe-derived EVs have recently moved into the spotlight for their ability to resemble the plant's therapeutic properties while acting as efficient, biocompatible nanocarriers. Preliminary studies suggest that they can regulate inflammatory signaling, activate antioxidant defenses, and prevent the differentiation and contractile activity of myofibroblasts.[35-37] Their versatility is further exemplified by

their applications in indocyanine green encapsulation for targeted melanoma therapy.[38] However, there remains a significant lack in the literature regarding the influence of extraction methodology and plant maturity on the biological efficacy of Aloe-derived EVs, and no comprehensive *in vitro* study has yet evaluated their concurrent ability to modulate oxidative stress, inflammatory responses, and fibrotic remodeling within the context of abnormal skin scarring.

Therefore, in this study, we report a comprehensive biological characterization of Aloe vera gel-derived extracellular vesicles (Av-EVs), with a focus on their capacity to modulate key pathological mechanisms underlying abnormal scar formation. Specifically, we investigated the ability of Av-EVs to attenuate pro-inflammatory cytokine expression in M1-polarized macrophages while promoting M2-like phenotype, suppress myofibroblast differentiation in human dermal fibroblasts, and reduce intracellular ROS levels – three interrelated processes central to fibrotic remodeling. To deepen our understanding of their therapeutic value, we systematically compared Av-EVs isolated via manual extraction (no blender, NB) versus shear-force homogenization (blender, B), and evaluated the influence of leaf maturity by comparing EVs derived from mature Aloe vera leaves (commercially-grade) and younger leaves from nursery-grown plants. This comparative framework provides critical insights into how source material and processing techniques affect the physicochemical and functional properties of Av-EVs, and positions them as promising, plant-based nanotherapeutics for the prevention and treatment of fibrosis-related skin disorders.

2. Materials and Approach

2.1 Av-EVs Isolation and Characterization

2.1.1 Av-EVs Isolation from Aloe vera Gel

Fresh Aloe vera *barbadensis miller* leaves from mature plants (Melissa's/World Variety Produce, Inc., USA) with similar appearance and dimensions (~67 cm long x ~9 cm wide x ~3 cm thick) were purchased from a local market. Note that the comparison between mature and young plants is described under 2.3.7. These mature leaves were cut and rinsed with distilled water until the mucilage was removed. Subsequently, the pointed ends and the anterior leaf skin were chopped with a sterilized knife to separate it from the transparent inner gel. After peeling, the extraction and homogenization of the Aloe vera gel was carried out employing a manual method (no blender, NB Av-EVs) and a shear force-based (blender, B Av-EVs) method. For the manual method, the gel was meticulously scooped out using a sterilized spoon, avoiding any inclusion of the yellow latex. A total of 400 mL of the extracted gel was transferred into a clean glass container where it was mixed with Dulbecco's phosphate-buffered saline (DPBS, Cytiva, USA, SH30028.02) in a 1:1 v/v ratio and homogenized using an orbital shaker (Chemglass CLS-4021-100 Versa-Orb, USA) at 100 rpm and 4 °C for 1 h. Then, the remaining solid residues were separated with a sterilized fine-mesh sieve. On the other hand, the entire transparent inner portion was removed from the posterior leaf skin and homogenized with 1:1 v/v ratio of DPBS using a commercial blender for the shear force-based method to obtain 800 mL of Aloe vera juice. In both cases, the soluble fractions were sequentially centrifuged (Centrifuge 5810, Eppendorf, USA) at 1,000 g for 10 min, 2,000 g for 20 min, 3,000 g for 30 min, and 15,000 g for 35 min at 4 °C to remove debris and larger particles. The supernatants were then ultracentrifuged (Optima™ MAX-XP Ultracentrifuge, Beckman Coulter®, USA) at 100,000 g

for 60 min at 4 °C and the resulting 6 pellets were resuspended and pooled in 10 mL of DPBS. The final suspensions containing the Av-EVs were filtered through a 0.22 µm filter (GVS, USA, FJ25BSCCA002AL01) and stored in aliquots of 1 mL at −80 °C until further use. The entire process was performed four times for each method, processing a total of 400 mL of Aloe vera gel and yielding four 10 mL batches of purified Av-EVs per ultracentrifugation cycle.

2.1.2 Nanoparticle Tracking Analysis

Particle concentration and size distribution were measured using nanoparticle tracking analysis (NTA, NanoSight NS300, Malvern Panalytical, UK). The samples were diluted 1:50 with DPBS to reach an optimal concentration for instrument linearity. Three videos of 30 s were captured with a camera level of 14 and measured with a detection threshold of 5. Data was processed with the NanoSight NTA 3.4 software.

2.1.3 Transmission Electron Microscopy

Transmission electron microscopy (TEM) was employed to verify vesicle structure, for which 3 mL of the Av-EVs preparation were spotted on formvar/carbon-coated copper grids with a 200-mesh size (Electron Microscopy Science, USA) following glow discharge for 30 s at 30 mA and incubation for 30 s. The excess sample was blotted, and grids were rinsed sequentially with molecular grade water and counterstained with 0.75% uranyl formate solution for 1 min. Grids were allowed to air dry before imaging them on a Talos L120C TEM equipped with a 16 MP CETA camera at 8,500 and 22 k magnification using the TIA software (Thermo Fisher Scientific, USA).

2.1.4 Protein Quantification

Pierce™ BCA protein assay kit (Thermo Scientific, USA, 23225) was used to quantify proteins that were either bound to the external surface of the Av-EVs or co-precipitated during the isolation process following the manufacturer's instructions for the standard protocol and microplate procedure. For each protein quantification assay, a single EV pellet – obtained from one of the six ultracentrifugation pellets produced during one Av-EV isolation cycle – was individually resuspended in 300 µL of DPBS. No pooling of multiple pellets was performed prior to protein analysis to ensure that concentration measurements reflected the yield per individual pellet.

Briefly, the diluted bovine serum albumin (BSA, 23209) standards were prepared using 0 – 400 µL of DPBS for a working range of 2,000 – 25 µg/mL. The working reagent (WR) was prepared by mixing reagent A (23228) and B (1859078) at a 50:1 ratio until obtaining a clear, green WR for a total of 9 standards, 6 Av-EV samples and 2 replicates. 10 µL of each standard and Av-EVs samples were pipetted into a clear 96-well plate and 200 µL of the WR were added to each well. The plate was thoroughly mixed on an orbital shaker for 30 s, covered with aluminum foil to protect it from direct light, and incubated at 37 ºC for 30 min. Afterward, the absorbance was read at 562 nm on a SpectraMax iD3® spectrophotometer equipped with the Softmax Pro 7 software (Molecular Devices, USA). Results were normalized to the blank standard measurement of DPBS, and the protein concentration of each Av-EV sample was determined based on the BSA standard curve.

2.2 Cell Cultures

2.2.1 THP-1 Culture and Differentiation into M0 Macrophages

Human leukemia monocytic type 1 (THP-1) cells (The American Type Culture Collection (ATCC), USA) were cultured in Roswell park memorial institute medium (RPMI 1640, Cytiva, USA, SH30255.01) supplemented with 10% fetal bovine serum (FBS, Cytiva, USA, SH30070.03), 1% anti-anti (A/A, Gibco™, USA, SV30079.01), and 1% sodium pyruvate (Gibco™, CN, 11360-070) at 2×10^5 cells/mL concentration under standard conditions (37 ºC with 5% CO_2). The cells were allowed to grow for two weeks with medium change every 2 – 3 days. Differentiation to macrophages (M0) was done by seeding the THP-1 cells into 24-well plates at 2×10^5 cells per well and adding 100 ng/mL of phorbol 24-myristate 13-acetate (PMA, Cayman Chemical, USA, 16561-29-8) with standard medium for 24 h until the cells were attached and attained a macrophage-like morphology. Following adhesion, the corresponding treatment was added, and the specific assay was performed.

2.2.2 hDFs Culture

Primary human dermal fibroblasts (hDFs), lot numbers 80405992 and 80124232 (ATCC, USA), were cultured in Dulbecco's modified eagle medium (DMEM, Cytiva, USA, SH30023.01) supplemented with 10% FBS and 1% A/A under standard conditions. To support cell proliferation and maintenance, 5 ng/mL fibroblast growth factor (FGF, PeproTech, USA, 100-18B) was freshly added to the culture medium with each media change. Cells were fed every 2 – 3 days and passaged using 1X Trypsin-EDTA (Gibco™, CA, 15400-054) upon reaching approximately 80% confluence, and only passages ≤ 5 were used for experiments. For all assays, 1.5×10^4 cells per well were seeded into 24-well plates and allowed to adhere for 24 hours. Following adhesion, the corresponding treatment was added, and the specific assay was performed.

2.3 Biological Effects of Av-EVs Cargo

2.3.1 Antioxidant Capacity

The antioxidant activity of Av-EVs was evaluated by measuring their ability to scavenge the free 2,2-diphenyl-1-picrylhydrazyl (DPPH) radical, using a DPPH antioxidant assay kit (Dojindo, USA, D678) following the manufacturer's protocol. Identical to the protein quantification assay, for each antioxidant analysis, a single EV pellet – obtained from one of the six ultracentrifugation pellets produced during one Av-EV isolation cycle – was individually resuspended in 300 µL of DPBS. No pooling of multiple pellets was performed.

Briefly, 20 µL of three (n=3) NB and B Av-EV samples obtained from separate isolation experiments under the same conditions were incubated at RT in the dark with 80 µL of assay buffer and 100 µL of DPPH working solution (WS) diluted in 99.5% molecular grade ethanol (Sigma-Aldrich, USA, SHBS1884). Additionally, DPPH + ethanol was used as negative control, and EVs in DPBS as sample blank. At time intervals of 1, 24, 48, and 72 h, absorbance was measured at 517 nm using the SpectraMax iD3® spectrophotometer. The DPPH radical scavenging activity (inhibition ratio %) of the samples was calculated using the following equation:

$$Inhibition\ ratio\ (\%) = \frac{A_{control} - (A_{sample} - A_{blank})}{A_{control}} \times 100$$

2.3.2 Cytotoxicity Assessment

Cell viability was assessed using alamarBlueTM cell viability reagent (InvitrogenTM by Thermo Fisher Scientific, USA, DAL1025). Briefly, 350 µL of freshly made working alamarBlue solution diluted at 10% in each corresponding standard medium was added to each well at the indicated time points and allowed to incubate under standard conditions for 3 h. The plate was wrapped with aluminum foil to protect it from direct light. Next, 200 µL of the supernatant from each well was transferred to a 96-well black plate with clear bottom (Corning Incorporated, USA, 3603) and fluorescence levels of the reduced resazurin were read on a SpectraMax iD3® spectrophotometer equipped with the Softmax Pro 7 software (Molecular Devices, USA). The excitation/emission wavelengths were set at 560/590, respectively. Results were normalized with a blank of 10% alamarBlue without cells and the statistical analysis was performed using the respective untreated conditions (i.e., –LPS/–EVs for macrophages or –TGFβ1–VitC/–EVs for fibroblasts) as controls.

2.3.3 Anti-inflammatory Response (Macrophages)

M0 macrophages were polarized to M1 macrophages through lipopolysaccharide (LPS, Sigma-Aldrich, USA, L6529-1MG) treatment. Fresh NB or B Av-EVs were added to serum-free medium simultaneously with 500 ng/mL of LPS and the treatment continued for 24 h, 72 h or 7 days. The experimental setup is specified in **Table 1**. D indicates different doses of EVs, where D1, D2, and D3 correspond to 1,000, 2,500, 5,000 Av-EVs per target cell, respectively. The term "EVs" is used throughout to describe particle concentrations measured by nanoparticle tracking analysis (NTA); however, it is important to note that not all particles quantified by NTA are necessarily extracellular vesicles. These measurements may include co-isolated nanoparticles such as protein aggregates or other vesicle-like structures. C-X-C motif chemokine ligand 10 (CXCL10) also known as Interferon gamma-induced protein 10 (IP-10), C-C motif chemokine ligand 2 (CCL2) also known as monocyte chemoattractant protein-1 (MCP-1), interleukin-1β (IL-1β), tumor necrosis factor alpha (TNF-α), interleukin-6 (IL-6), interleukin-10 (IL-10), interleukin-13 (IL-13), and arginase 1 (ARG1) expression was quantified by RT-qPCR to analyze the anti-inflammatory potential of Av-EVs and their capacity to modulate macrophage polarization from M1 to M2 phenotype (see details in 2.4.1).

Table 1. *Experimental setup for the anti-inflammatory response.*

Condition	Explanation
–LPS / –EVs	Untreated control
+LPS / –EVs	Pro-inflammatory positive control
–LPS / +NBEVs	NB Av-EVs control
–LPS / +BEVs	B Av-EVs control
+LPS / +NBEVs D1	LPS and 1,000 NB AV-EVs / cell
+LPS / +NBEVs D2	LPS and 2,500 NB AV-EVs / cell
+LPS / +NBEVs D3	LPS and 5,000 NB AV-EVs / cell
+LPS / +BEVs D1	LPS and 1,000 B AV-EVs / cell
+LPS / +BEVs D2	LPS and 2,500 B AV-EVs / cell
+LPS / +BEVs D3	LPS and 5,000 B AV-EVs / cell

2.3.4 Antifibrotic Response (Dermal Fibroblasts)

TGF-β1 (PreproTech, USA, 100-21) and vitamin C (L-Ascorbic acid, Sigma-Aldrich, USA, A8960-5G) treatment was used to induce healthy hDFs transdifferentiation of fibroblasts to myofibroblasts, a recognized indicator of fibrosis. In brief, healthy hDFs were expanded and seeded as described in section 2.2.2. Once the cells were attached to the wells, the standard medium was replaced with fresh medium with 2.5% FBS + 10 ng/ml TGFβ1 + 100 μM vitamin C. Fresh NB or B Av-EVs were added simultaneously and the treatment continued for 72 h. The experimental setup is specified in **Table 2**. Identical to macrophages, D1, D2 and D3 were 1,000, 2,500, 5,000 NB or B Av-EVs per target cell, respectively. The expression of collagen type I (COL1A1) and α-SMA, also known as actin alpha 2 (ACTA2) was quantified by RT-qPCR to analyze the antifibrotic potential of Av-EVs and their capacity to modulate myofibroblast differentiation. Additionally, immunofluorescence microscopy was used for α-SMA protein visualization (see details in 2.4.1 and 2.4.2).

Table 2. *Experimental setup for the antifibrotic response.*

Condition	Explanation
–TGFβ1-VitC / –EVs	Untreated control
+TGFβ1+VitC / –EVs	Fibrotic positive control
–TGFβ1–VitC / +NBEVs	NB Av-EVs control
–TGFβ1–VitC / +BEVs	B Av-EVs control
+TGFβ1+VitC / +NBEVs D1	TGFβ1/VitC and 1,000 NB AV-EVs / cell
+TGFβ1+VitC / +NBEVs D2	TGFβ1/VitC and 2,500 NB AV-EVs / cell
+TGFβ1+VitC / +NBEVs D3	TGFβ1/VitC and 5,000 NB AV-EVs / cell
+TGFβ1+VitC / +BEVs D1	TGFβ1/VitC and 1,000 B AV-EVs / cell
+TGFβ1+VitC / +BEVs D2	TGFβ1/VitC and 2,500 B AV-EVs / cell
+TGFβ1+VitC / +BEVs D3	TGFβ1/VitC and 5,000 B AV-EVs / cell

2.3.5 Cellular Uptake of Av-EVs

To visualize the cellular uptake of Av-EVs, vesicles were labeled using the PKH26 red fluorescent membrane kit (Sigma–Aldrich, USA, 4103849473) (panel: red). After isolation, 10 mL of purified Av-EVs in DPBS were stored in aliquots at −80 °C as previously described. For PKH26 labeling, one 1 mL aliquot was thawed and ultracentrifuged at 100,000 g and 4 °C for 60 min. The pellet was then resuspended in 1 mL of Diluent C. Separately, 4 μL of PKH26 ethanolic dye solution was mixed in 1 mL of Diluent C until complete dispersion. Then, the Av-EVs suspension was mixed in the dye solution and incubated at room temperature (RT) for 10 min. An equal volume (2 mL) of 10% FBS in DMEM was added to stop the labeling reaction. Finally, the solution was ultracentrifuged, and the resulting pellet was washed with DPBS and ultracentrifuged one more time to remove free dye aggregates. The final pellet containing the labeled Av-EVs was resuspended in the initial volume of DPBS (1 mL), wrapped in aluminum foil to protect from light and stored at −20 °C until further use.

THP-1 and hDFs were seeded in their respective standard medium and left to adhere for 24 h, as described in sections 2.2.1 and 2.2.2. Following attachment, cells were stimulated according to the protocols detailed in sections 2.3.3 and 2.3.4. to induce either M1 macrophage polarization (via LPS) or fibroblast to myofibroblast differentiation (via TGF-β1/vitamin C), respectively. Simultaneously, cells were treated with PKH26-labeled Av-EVs at the highest dose (D3: 5,000 EVs/cell) and incubated for an additional 24 h to allow for vesicle uptake. Subsequently, the cells were fixed with 4% paraformaldehyde solution (Thermo Scientific, USA, J19943-K2) at RT for 15 min, permeabilized with 1X PBS-Triton X-100 (Alfa

Aesar, USA, J63521) at RT for 15 min, and blocked with 4% BSA (Thermo Scientific Chemicals, USA, AAJ6410009) in DPBS at 4 ºC for 2 h. From this point on, all procedures were carried out under low-light conditions to protect the fluorescent dyes. The Alexa Fluor™ 488 phalloidin (Invitrogen, USA, A12379) was diluted 1:400 in 4% BSA and added to the cells to stain the actin filaments (F-actin) at RT for 30 min (panel: green), followed by Hoechst 33342 (Thermo Scientific, USA, H3570) staining to label cell nuclei at a dilution of 1:3,000 in DPBS at RT for 5 min (panel: blue). Finally, the cells were washed and visualized under fluorescence microscopy (Olympus IX81, USA) to confirm the cellular uptake of PKH26-labeled Av-EVs and evaluate cytoskeletal and nuclear features. The images were captured at 20X and 40X magnifications and processed using FIJI (Image J) software.

2.4 Analysis of Cell Responses to Av-EVs from Mature Aloe vera Leaves

2.4.1 Gene Expression

Reverse transcription-quantitative polymerase chain reaction (RT-qPCR) was employed to investigate the anti-inflammatory potential of Av-EVs using THP-1 macrophages stimulated with LPS by analyzing the gene expression of human pro-inflammatory (CXCL10/IP-10, CCL2/MCP-1, IL-1β, TNF-α, IL-6) and anti-inflammatory (IL-10, IL-13) cytokines, as well as the expression of ARG1, an enzyme highly expressed in M2a macrophages. Additionally, RT-qPCR served to investigate the hDFs transdifferentiation into myofibroblast after treatment with TGF-β1 and vitamin C by analyzing the gene expression of COL1A1 and α-SMA/ACTA2. The ID of each primer can be found in **Table 3**.

Total RNA was extracted from THP-1-derived macrophages and hDFs using the RNeasy mini kit (Qiagen, DE, 74106) according to the manufacturer's protocol. RNA concentration and purity were assessed spectrophotometrically using a NanoPhotometer® N50 (Implen, DE), and yields were expressed in ng/µL. Subsequently, RNA was reverse transcribed into complementary DNA (cDNA) using the high-capacity cDNA reverse transcription kit with RNase inhibitor (Applied Biosystems™ by Thermo Fisher Scientific, USA, 4374967) on a T100™ thermal cycler (Bio-Rad, USA). Quantitative real-time PCR (qPCR) was then performed using TaqMan™ fast advanced master mix (Applied Biosystems™, USA, 4444557) with gene-specific primers (Applied Biosystems™, USA, 4331182) on a QuantStudio™ 3 Real-Time PCR System (Applied Biosystems™, USA). Gene expression levels were quantified by the ΔΔCt method represented in terms of fold change ($2^{-\Delta\Delta Ct}$). The TATA-binding protein (TBP) gene served as the endogenous reference. Experimental conditions were normalized to their respective stimulated controls: +LPS/–EVs for pro-inflammatory assays and +TGF-β1+VitC/–EVs for fibrotic assays. All qPCR reactions were conducted in duplicate for each gene and treatment group.

Table 3. *TaqMan™ gene expression assays used for RT-qPCR analysis.*

Primer Name	Primer ID
TBP	Hs00427620_m1
CXCL10	Hs00171042_m1
CCL2	Hs00234140_m1
IL-1β	Hs01555410_m1
TNF-α	Hs00174128_m1
IL-6	Hs00174131_m1
IL-10	Hs00961622_m1
IL-13	Hs00174379_m1

ARG1	Hs00163660_m1
COL1A1	Hs00164004_m1
ACTA2	Hs00426835_g1

2.4.2 Smooth Muscle Actin Immunofluorescence Analysis

To analyze α-SMA protein expression in fibrotic hDFs treated with the intermediate dose (2,500 EVs/cell) of either NB- or B-derived Av-EVs (as described in section 2.3.4), immunofluorescence staining was performed. The cells were seeded, differentiated, fixed, permeabilized and blocked as described in section 2.3.5. Then, the cells were incubated with alpha-smooth muscle actin monoclonal antibody (1A4), eBioscience™ (Invitrogen, USA, 14-9760-82) at 1 µg/mL in 0.1% BSA at 4 ºC overnight and then labeled with goat anti-mouse IgG (H+L) superclonal™ secondary antibody, Alexa Fluor 488™ conjugate (Invitrogen, USA, A28175) at a dilution of 1:2000 at RT for 45 min (panel: green). Afterward, F-actin was stained with Alexa Fluor™ 594 phalloidin (Invitrogen, USA, A12381) diluted 1:400 in 4% BSA at RT for 30 min (panel: red), and nuclei were stained with Hoechst 33342 (panel: blue). For each condition, three independent images were acquired at 20X magnification under identical exposure settings to enable objective comparison of fluorescence intensity. From each image, two regions of interest were analyzed, yielding a total of six α-SMA and six background pixel intensity measurements per group. Quantification was performed using FIJI (ImageJ) software by calculating net α-SMA signal intensity as the difference between each α-SMA measurement and the average background value. To enhance visualization while preserving quantitative accuracy, uniform brightness and contrast adjustments were applied post-capture across all images.

2.5 Comparative Analysis of NB Av-EVs Isolated from Mature and Young Aloe vera Leaves

2.5.1 Gene Expression

To assess the influence of plant maturity on the biological activity and protein composition of Av-EVs, we extended our investigation to include EVs manually extracted from young Aloe vera *barbadensis miller* leaves. These leaves were harvested from live potted plants purchased at a local plant shop and the EVs were isolated using the same manual protocol previously described in section 2.1.1. Following isolation, the anti-inflammatory potential of young versus mature NB Av-EVs was evaluated in THP-1-derived macrophages after 24 hours of co-treatment. Gene expressions of CXCL10/IP-10, CCL2/MCP-1, IL-1β, TNF-α, IL-6, and IL-10 were analyzed by RT-qPCR. In parallel, the antifibrotic response was assessed in hDFs by quantifying COL1A1 and α-SMA/ACTA2 expression levels. Importantly, due to the independent experimental setup for mature and young Aloe vera EVs, separate untreated and stimulated control groups were used to ensure proper normalization and comparison within each batch.

2.6 Statistical Analysis

Experiments were performed in six biological replicates (n=6) unless otherwise stated and data were represented as means ± standard deviations (SD). Normality was evaluated with the Shapiro-Wilk test. Statistical difference was assessed with student's t-test, one-way or two-ways analysis of variance (ANOVA) followed by Tukey's post-hoc comparison or Geisser-Greenhouse's epsilon correction,

respectively. Significance was considered for p values < 0.05. Analyses were performed using GraphPad Prism version 10.4.2 (GraphPad Software, USA).

3. Results and Discussion

3.1 Av-EVs Isolation and Characterization

Extracellular vesicles from Aloe vera gel (Av-EVs) were isolated using two protocols: a gentle manual homogenization approach (NB Av-EVs) and a shear force-based method using a commercial blender (B Av-EVs), as illustrated in **Figure 1A**. All vesicle preparations were characterized in accordance with the MISEV2023 guidelines established by the International Society for Extracellular Vesicles (ISEV).[39] Characterization was conducted on four independent replicates for each method.

Nanoparticle tracking analysis (NTA) established that all final suspension samples consistently yielded concentrations ranging from 1.4 to 2.0 × 10^{10} particles/mL, for an average total of 5.6 to 8 × 10^{11} particles per leaf. Furthermore, they displayed heterogeneous size distributions with mean diameters between 150 – 250 nm [**Figure 1B**], consistent with previous reports on Aloe-derived EVs.[35-37, 40] While this overall range was reproducible across both methods, NB EVs typically clustered between 1.4 to 1.6 × 10^{10} particles/mL, whereas B-derived EVs approached 1.8 to 2.0 × 10^{10} particles/mL. The disparity may reflect the influence of shear stress introduced by blender homogenization, which could not only liberate vesicles already present in the inner parenchyma but also mobilize vesicles from within vacuoles or induce vesiculation through mechanical disruption. This hypothesis is supported by literature describing how laminar or turbulent shear flow can destabilize lipid membranes, promoting membrane budding or fragmentation. Such mechanical stress can cause intracellular content leakage and drive the spontaneous formation of EV-like vesicles, often diverse in size and composition.[41]

Transmission electron microscopy (TEM) verified the presence of rounded, membrane-bound vesicles with well-defined lipid bilayers – characteristic of EVs. The morphology observed in both NB and B Av-EVs groups supports the preservation of vesicle integrity following isolation, regardless of the extraction method used. Nonetheless, notable differences in size distribution were evident as expected: B-derived Av-EVs displayed a broader range of diameters (approximately 70 to 170 nm), whereas NB-derived EVs showed a more uniform morphology, with most imaged vesicles falling near the upper size range observed by NTA (~250 nm). While some vesicles measured closer to 300 nm in TEM, this discrepancy may be attributed to swelling or flattening during sample preparation and imaging, a known artifact in conventional TEM workflows. These observations align with NTA results and further support the idea that blender-induced shear stress promotes vesicle heterogeneity, potentially generating a mixture of natural and mechanically derived vesicles.

Protein quantification results provide further evidence of the impact of extraction methods [**Figure 1C**]. NB-derived EVs exhibited consistent protein concentrations across independently processed leaves, ranging from 159 to 198 µg/mL, corresponding to a total protein yield of 3,816 to 4,752 µg per leaf. In contrast, B-derived EVs showed substantial inter-replicate variability, with concentrations spanning 160 to 447 µg/mL and a total protein yield of 3,840 to 10,728 µg per leaf. Statistical analysis confirmed a significant difference in total protein levels between the NB and B groups ($p < 0.05$), suggesting that the shear-based method may produce a more heterogeneous population of vesicles, potentially including non-physiological particles or protein-rich artifacts. However, when protein levels were normalized to the total

EV yield per leaf, both methods exhibited relatively consistent protein-to-particle ratio. NB-derived EVs ranged from 6.81 to 7.43 × 10^{-9} µg/EV, while B-derived EVs ranged from 5.33 to 13.41 × 10^{-9} µg/EV. Despite the higher variability observed in the raw protein concentration of B samples, the differences between the two groups became less pronounced after normalization, indicating that the protein content per EV remains relatively similar across both EV types.

In summary, both isolation protocols were successful in yielding Av-EVs that meet established EV characterization criteria in terms of size, concentration, and morphology. However, the manual method yielded more uniform vesicle populations with slightly lower protein variability, suggesting greater preservation of native EV characteristics and reduced likelihood of shear-induced artifacts.

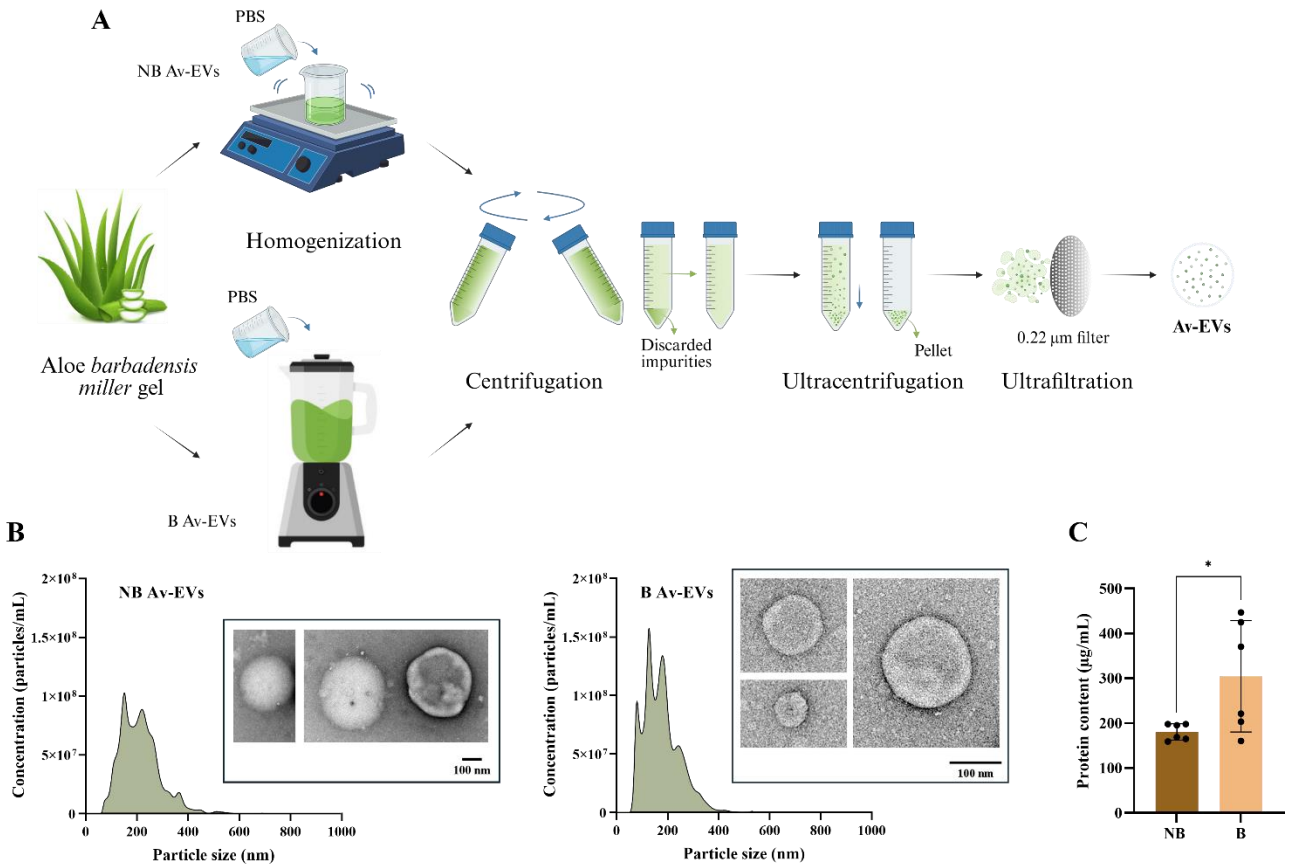

Figure 1. (A) *Schematic illustration of NB and B Av-EV isolation procedures from Aloe vera barbadensis miller leaves.* ***(B)*** *NTA data showing size distribution of typical NB and B Av-EV samples with their respective TEM images.* ***(C)*** *Protein content data represents the mean ± SD with n=6 and p < 0.05 *.*

3.2 Biological Effects of Av-EVs Cargo from Mature Aloe vera Leaves

3.2.1 Antioxidant Capacity

The antioxidant potential of Av-EVs was evaluated using the DPPH radical scavenging assay, a widely accepted method that quantifies a compound's ability to neutralize free radicals via electron or hydrogen atom donation. In this assay, decreased DPPH absorbance correlates with increased antioxidant activity, expressed as the DPPH inhibition ratio (%). Both NB and B Av-EVs were tested at four concentrations

(5×10^8, 1×10^9, 5×10^9, and 2×10^{10} EVs/mL) and assessed at four time points (1, 24, 48, and 72 hours) to evaluate both dose- and time-dependent antioxidant dynamics.

As shown in **Figure 2**, all Av-EV treatment groups demonstrated a clear time-dependent increase in DPPH inhibition, indicative of progressive and sustained antioxidant activity. During the first hour, all samples – regardless of dose or method – exhibited relatively uniform inhibition values (~20 – 40%), suggesting similar initial redox interactions. By 24 hours, B-derived EVs maintained modest inhibition levels (20 – 40%), whereas some NB-derived EV replicates began to display more pronounced scavenging effects, reaching inhibition values of up to ~80%. Notably, greater variability emerged across replicates between the 24 and 48 h window, potentially reflecting differences in cargo release kinetics, vesicle stability, or vesicle–radical interaction. Despite this fluctuation, the antioxidant response became more consistent by 72 hours, with nearly all treatment conditions – especially those involving NB EVs – stabilizing at high inhibition levels (> 90%).

Statistical analysis confirmed a significant increase in inhibition from 1 to 48 hours for NB EVs at both 5×10^9 and 2×10^{10} EVs/mL ($p < 0.01$ and $p < 0.05$, respectively), and from 1 to 72 hours ($p < 0.001$ and $p < 0.05$, respectively). In contrast, B-derived EVs at the same concentrations reached significance only between 1 and 72 hours ($p < 0.05$). Furthermore, even the lowest NB EV dose (5×10^8 EVs/mL) showed a significant increase between 24 and 48 hours ($p < 0.001$). These findings underscore the sustained redox-modulatory capacity of Av-EVs and suggest that NB-derived vesicles may deliver more timely and effective antioxidant action.

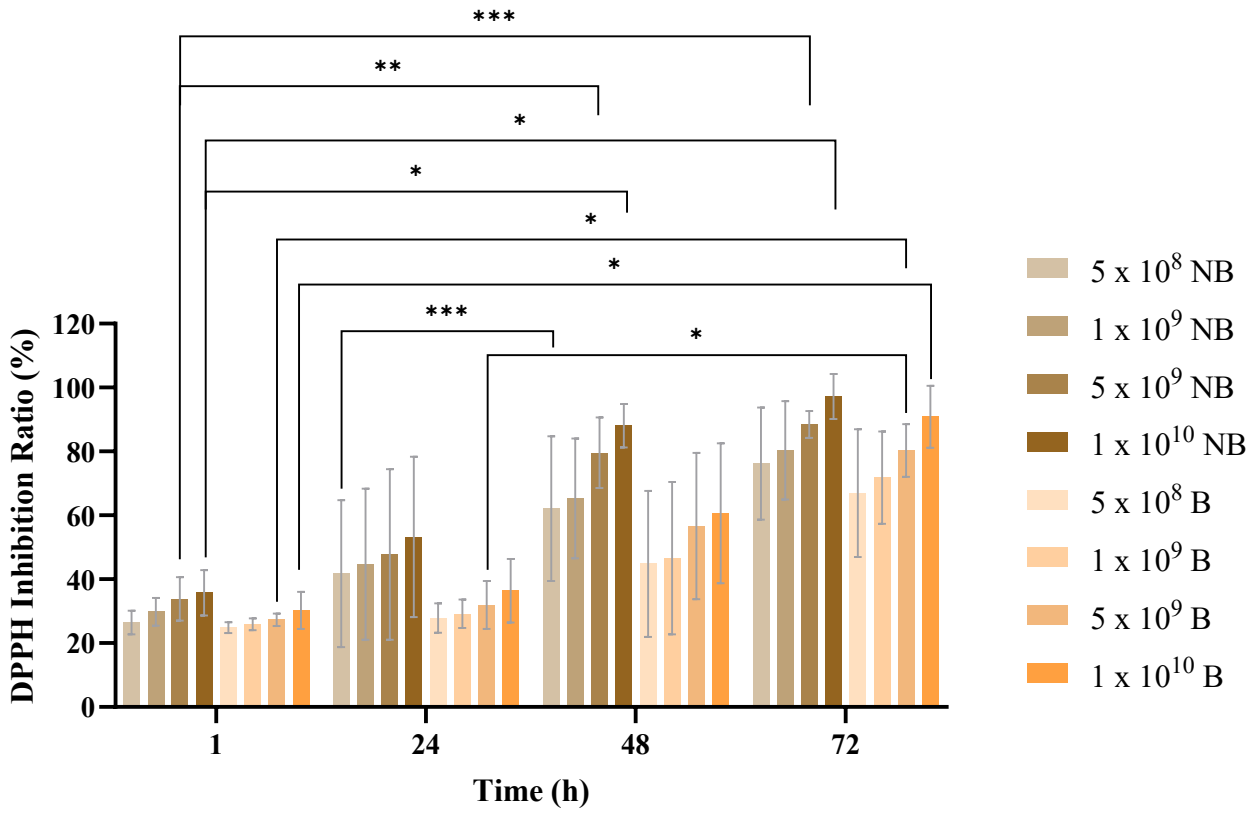

Figure 2. *DPPH inhibition ratio (%) over time for NB and B Av-EVs at four concentrations (5×10^8, 1×10^9, 5×10^9, and 2×10^{10} EVs/mL). Inhibition data represents the mean ± SD with n=3 and $p < 0.05$ *, < 0.01 **, < 0.001 ***.*

Additionally, although statistical significance was not observed across all comparisons, a consistent dose-dependent trend was observed: the highest concentration (2×10^{10} EVs/mL) yielded the strongest DPPH inhibition at each time point, whereas the lowest concentration (5×10^{8} EVs/mL) produced the weakest response. This pattern reinforces the premise that the antioxidant efficacy of Av-EVs is proportional to the concentration of vesicle-delivered bioactive compounds. Interestingly, across all tested doses, NB-derived EVs achieved greater inhibition ratios than their B-derived counterparts. This superior performance, even at lower concentrations, highlights the importance of gentle manual extraction methods in preserving vesicle integrity and maximizing functional antioxidant potential.

This antioxidant efficacy is aligned with the well-documented phytochemical profile of Aloe vera, which includes a variety of redox-active molecules such as α-tocopherol (vitamin E), ascorbic acid (vitamin C), carotenoids, polyphenols (flavonoids and tannins), indoles, alkaloids, and anthraquinones (e.g., aloin and aloe-emodin).[22, 42-44] Additionally, the plant contains enzymatic antioxidants such as superoxide dismutase (SOD) and glutathione peroxidase (GPx), which contribute to ROS detoxification.[22] Prior studies have confirmed Aloe gel's ability to scavenge free radicals such as DPPH, ABTS, and NO in a concentration-dependent manner, inhibit lipid peroxidation, and protect against oxidative damage.[23] Furthermore, it has been shown to modulate oxidative stress pathways, including the inhibition of the NOX4/ROS/p38 signaling axis,[45] thereby preventing the activation of latent TGF-β1 and the fibrogenic transformation of fibroblasts and endothelial cells into α-SMA-positive myofibroblasts. Recent research on Aloe-derived EVs also supports their role in delaying skin photoaging via activation of the Nrf2/ARE pathway – a key cellular defense mechanism – along with reductions in H_2O_2 levels,[37] suppression of senescence-associated secretory phenotypes (SASP), and decreased malondialdehyde (MDA) in both *in vitro* and *in vivo* models.[40]

Given this extensive redox-modulatory background, the observed antioxidant effects of Av-EVs not only validate their bioactivity but also position them as promising natural nanocarriers for oxidative stress regulation. Since elevated intracellular ROS levels deplete endogenous defenses and perpetuate chronic inflammation, impaired wound healing, and fibrosis, the ability of Av-EVs to mitigate oxidative damage in a sustained, dose-responsive manner is particularly significant. By neutralizing ROS, Av-EVs may disrupt the positive feedback loop between oxidative stress and TGF-β1 signaling, ultimately aiding in the resolution of inflammation and prevention of pathological scar formation such as hypertrophic scars and keloids.

3.2.2 Cytotoxicity Assessment

Cell viability, defined as the ability of cells to maintain both functional integrity and proliferative potential, was assessed using the alamarBlue assay, which measures metabolic activity through the reduction of resazurin to fluorescent resorufin by intracellular oxidoreductases in metabolically active cells. This assay provides an integrative measure of cell viability by reflecting plasma membrane integrity, glycolytic flux, mitochondrial respiratory chain activity, and biosynthetic capacity. To evaluate the biocompatibility and potential cytotoxicity of NB and B Av-EVs, the alamarBlue assay was applied to both THP-1-derived macrophages and hDFs exposed to inflammatory or fibrotic stimuli, respectively. Untreated cells served as controls for statistical analysis (–LPS/–EVs or –TGF-β1–VitC/–EVs), and Av-EVs were administered at increasing doses (1,000, 2,500, and 5,000 EVs/cell) to assess their effects on cellular metabolism and viability across both the anti-inflammatory and antifibrotic experimental timelines.

THP-1-derived macrophages were activated using LPS, the major outer membrane component of Gram-negative bacteria, with or without Av-EV co-treatment. As shown in **Figure 3**, LPS alone significantly increased macrophage metabolic activity at 24 h, 72 h, and 7 days compared to the untreated control. Moreover, cotreatment with LPS and Av-EVs further enhanced metabolic activity at 24 and 72 hours across all doses and isolation methods, a period during which cells are expected to exhibit full M1 polarization and heightened inflammatory function. These findings confirm that Av-EVs do not exert cytotoxic effects and that macrophages remain metabolically viable under all treatment conditions.

The moderate decline in metabolic activity observed between 72 hours and day 7 suggests that Av-EVs facilitate a phenotypic transition from M1 to M2/M2a macrophages, consistent with the expected resolution phase of inflammation as confirmed with the gene expression data later (see section 3.2.4). This phenotypic shift from a pro-inflammatory to a reparative state is not only defined by cytokine expression profiles but also by fundamental metabolic reprogramming. M1 macrophages depend on aerobic glycolysis for rapid ATP production and biosynthesis to support inflammatory signaling, ROS generation, and cytokine secretion.[46-49] In contrast, M2 macrophages rely on oxidative phosphorylation (OXPHOS) and fatty acid oxidation (FAO), to support their anti-inflammatory and tissue-remodeling functions, which are energetically more efficient but generate fewer reduced equivalents.[46-49] Since the alamarBlue assay detects metabolic activity via NADH/NADPH-linked reduction of resazurin,[50] glycolytic M1 cells typically yield stronger signals than OXPHOS-driven M2 cells. Therefore, a decrease in alamarBlue signal at later time points under M2-polarizing conditions, such as Av-EV treatment, likely reflects a metabolic adaptation rather than cytotoxicity. Importantly, the dose-dependent nature of this effect – particularly the notable reduction at 5,000 EVs/cell – suggests that higher concentrations of Av-EVs may more strongly influence macrophage polarization and promote the initiation of tissue repair.

It is also noteworthy that *in vitro*, THP-1-derived macrophages naturally undergo reduced viability over time due to nutrient depletion, lack of stromal survival factors, and activation of intrinsic apoptotic pathways.[51] Similarly, *in vivo* M1 macrophages are generally short-lived, undergoing apoptosis or efferocytosis during the resolution of inflammation, while M2-polarized macrophages – particularly the M2a subtype – tend to persist longer due to their reparative and homeostatic roles.[52]

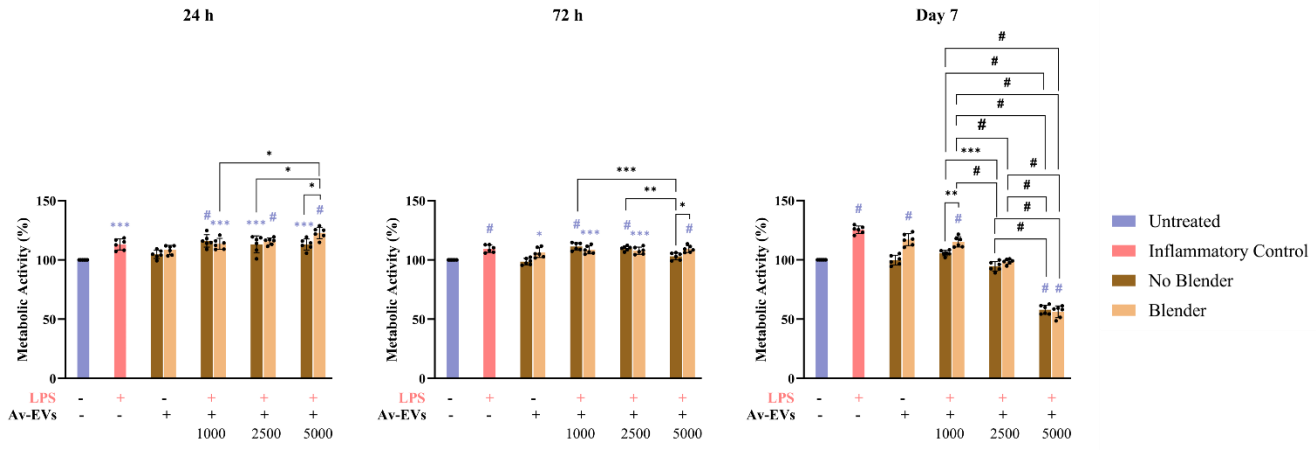

Figure 3. *Metabolic activity percentage in LPS-induced macrophages after 24 h, 72 h, and 7 days of co-treatment with No Blender or Blender Av-EVs at increasing doses (1,000, 2,500, 5,000 EVs/cell). Fluorescent data represents the mean ± SD with n=6 and p < 0.05 *, < 0.01 **, < 0.001 ***, < 0.0001 #. Statistical differences relative to untreated control (-LPS/-EVs) are shown in purple, while statistical differences between the isolation methods and doses are shown in black.*

To evaluate the metabolic impact and biocompatibility of Av-EVs on hDFs under fibrotic stimulation, the alamarBlue assay was performed following a 72-hour exposure to TGF-β1 and vitamin C, with or without Av-EV co-treatment. **Figure 4** shows that all groups exposed – including the fibrotic control and the Av-EV co-treated conditions – had a significant increase in metabolic activity compared to the untreated control. This increase reflects the transition from a quiescent fibroblast state to an activated phenotype. In this regard, resting hDFs exhibit low metabolic demand, relying mainly on basal mitochondrial respiration to support ECM maintenance and structural stability. Upon stimulation, activated fibroblasts display increased proliferation, migration, and biosynthesis – particularly of collagen and fibronectin – accompanied by enhanced glycolysis and mitochondrial oxidative metabolism.[53, 54] These shifts led to a measurable rise in cellular redox activity, as detected by the assay.

However, gene expression analysis and immunofluorescence later revealed that, despite similar metabolic activity across all conditions exposed to TGF-β1 and vitamin C, Av-EV co-treatment significantly suppressed the expression of key fibrotic markers such as COL1A1 and α-SMA, indicating a functional uncoupling between metabolic activity and fibrotic gene expression. This distinction is critical, as elevated metabolic activity alone does not necessarily equate to pathological transdifferentiation into myofibroblasts. Rather, Av-EVs may support a metabolically active yet functionally restrained fibroblast phenotype, in which the cells retain viability and activity but are prevented from progressing into a fully pro-fibrotic myofibroblast state, unlike those in the +TGFβ1+VitC/–EVs group.

Collectively, these findings confirm that Av-EVs are non-cytotoxic to both macrophages and hDFs across multiple time points and concentrations, validating their biocompatibility for immunomodulatory applications and supporting their potential use in prolonged treatment regimens aimed at modulating inflammation and preventing fibrosis.

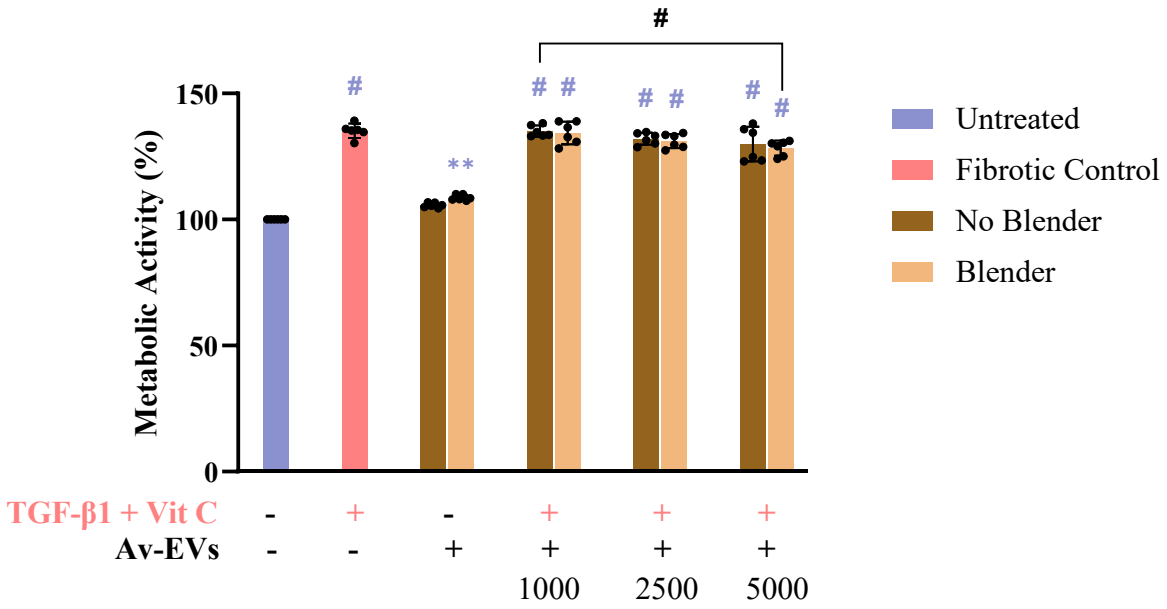

Figure 4. *Metabolic activity percentage in TGF- β1 + vitamin C- activated hDFs after 72 h co-treatment with No Blender or Blender Av-EVs at increasing doses (1,000, 2,500, 5,000 EVs/cell). Fluorescent data represents the mean ± SD with n=6 and p < 0.01 **, < 0.0001 #. Statistical differences relative to the untreated control (-TGFβ1-VitC/-EVs) are shown in purple, while statistical differences between the isolation methods and doses are shown in black.*

3.2.3 Cellular Uptake of Av-EVs

To confirm cellular uptake, THP-1 and hDFs cells were incubated with the highest dose (D3: 5,000 EVs/cell) of PKH26-labeled Av-EVs and subsequently analyzed by fluorescence microscopy. The results clearly demonstrate that both macrophages and dermal fibroblasts successfully internalized Av-EVs within 24 hours without compromising cell morphology, cytoskeletal organization, or viability, even under inflammatory or fibrotic activation.

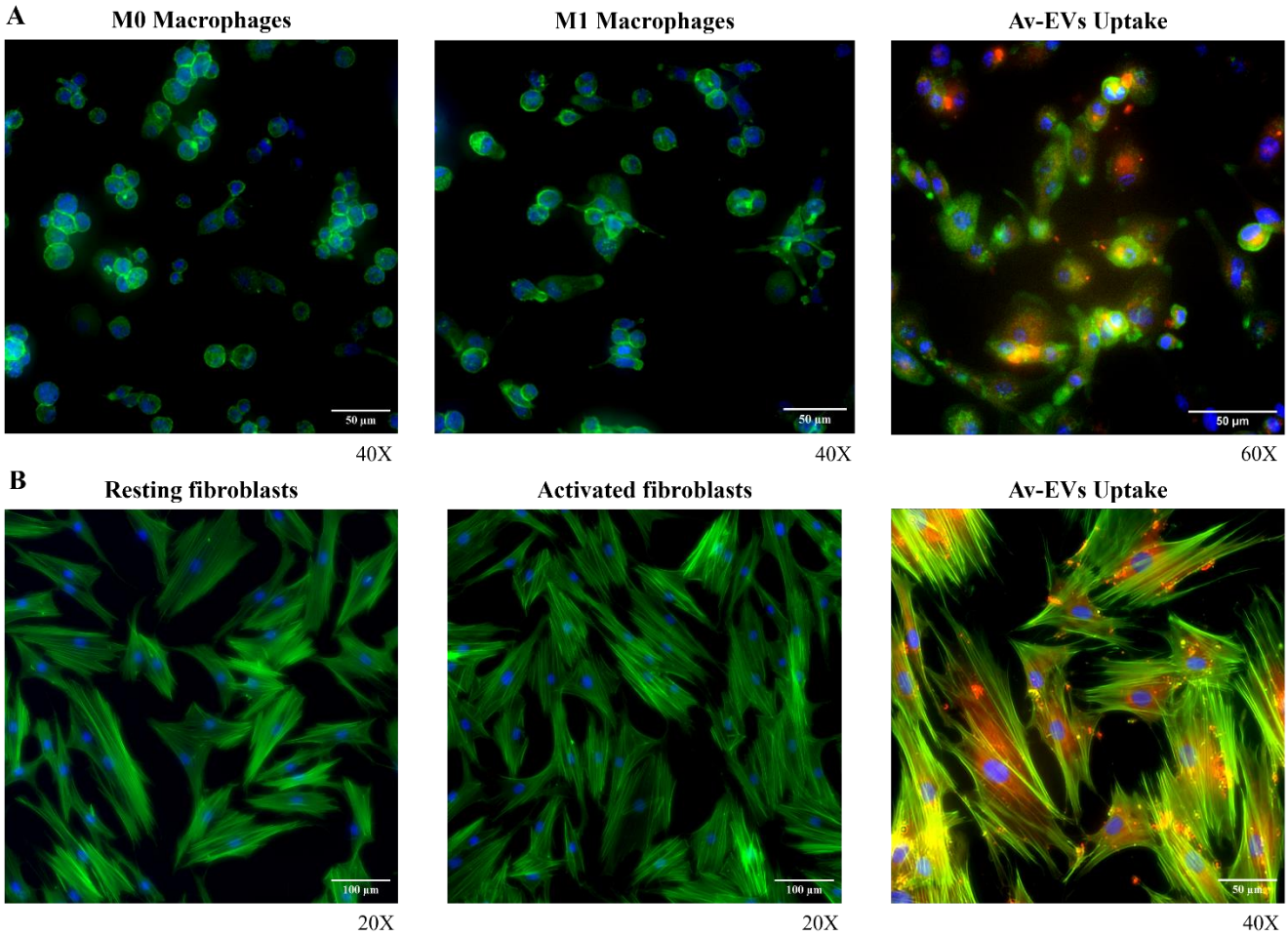

Figure 5. A. *From left to right: M0 macrophages, activation of M0 macrophages with LPS to induce M1 polarization, and cellular uptake of Av-EVs into M1 macrophages.* ***B.*** *From left to right: resting hDFs, activation of hDFs with TGF-β1 and vitamin C, and cellular uptake of AS-EVs into activated hDFs. PKH26 red fluorescent dye-labeled Av-EVs (red), F-actin (green), and nuclei (blue).*

Figure 5A presents the morphological features of macrophages across different conditions. M0 macrophages displayed a rounded shape, a diffuse cytoplasmic actin network, and clustered nuclei, consistent with a resting, non-polarized phenotype. F-actin was sparsely distributed and mainly localized at the cell periphery, indicating minimal cellular spreading. In contrast, LPS-stimulated macrophages (M1) showed a marked morphological shift, adopting an elongated, stellate shape with prominent stress fibers and lamellipodia, characteristic of M1 polarization. These cytoskeletal changes reflect enhanced motility and phagocytic readiness, driven by pro-inflammatory signaling. Macrophages treated with PKH26-labeled Av-EVs maintained this activated morphology but exhibited distinct red fluorescent signals localized within the perinuclear and cytoplasmic regions, confirming efficient uptake of the vesicles. This internalization, along with preserved cell structure and consistent metabolic activity from viability assays, indicates successful delivery of functional bioactive cargo capable of modulating the expression of both

pro- and anti-inflammatory cytokines, as later confirmed in the anti-inflammatory response experiment (see section 3.2.4).

Figure 5B shows the progression of fibroblast morphology following activation and Av-EV treatment. Resting fibroblasts exhibited the expected spindle-shaped appearance, with elongated nuclei and well-organized, parallel actin filaments aligned along the cell's longitudinal axis. These features are typical of quiescent fibroblasts that contribute to ECM maintenance under physiological conditions. After treatment with TGF-β1 and vitamin C, cells adopted a broader, more spread-out shape, with increased density and alignment and intensified F-actin staining, indicating the early stages of fibroblast-to-myofibroblast transdifferentiation. In cells exposed to PKH26-labeled Av-EVs, this activated morphology and cytoskeletal structure was retained, further confirming the non-cytotoxic and non-disruptive nature of Av-EV internalization. Importantly, bright red fluorescent signals were clearly visible, particularly in the perinuclear zones, indicating efficient vesicle uptake and intracellular delivery cargo capable of modulating gene expression of key fibrotic markers such as COL1A1 and α-SMA as later confirmed in the antifibrotic response experiment (see section 3.2.5).

3.2.4 Anti-inflammatory Response (Macrophages)

Two isolation protocols were compared to assess whether mechanical homogenization of Aloe vera gel alters the biological efficacy of the resulting vesicles. Both NB and B EVs were purified using identical centrifugation and ultracentrifugation workflows, ensuring comparability. THP-1 monocytes were differentiated into macrophages and further induced with LPS to adopt a proinflammatory M1 polarity, while being exposed to cotreatment with Av-EVs. The experimental conditions were as stated in **Table 1**.

Suppression of Pro-inflammatory Cytokines Expression at 24 Hours

RT-qPCR analysis of LPS-induced THP-1-derived macrophages revealed a robust upregulation of pro-inflammatory cytokines, including CXCL10/IP-10, CCL2/MCP-1, IL-1β, TNF-α, and IL-6 compared to untreated controls, consistent with classical M1 macrophage polarization [**Figure 6**]. In contrast, cotreatment with Av-EVs significantly attenuated this pro-inflammatory profile within 24 h, in a dose- and preparation-dependent manner. Notably, Av-EV control groups did not induce cytokine expression, with levels remaining near baseline, confirming that Av-EVs do not activate macrophages under homeostatic conditions.

Among the suppressed genes, CXCL10/IP-10 – a chemokine induced by IFN-γ and LPS that promotes Th1 responses and recruits activated T cells and macrophages – was significantly downregulated. Similarly, CCL2/MCP-1, a critical chemokine for monocyte recruitment and a well-established marker of M1-type polarization, was also strongly inhibited. Both NB and B Av-EVs significantly reduced the expression of CXCL10 and CCL2 in a dose-responsive manner, with near-complete suppression observed at the highest dose (D3, 5000 EVs/cell). Specifically, CXCL10 expression was reduced to a fold change of ≤ 0.017 (NB) and 0.059 (B), while CCL2 was suppressed to ≤ 0.017 (NB) and 0.021 (B). Even at the lowest dose (D1, 1000 EVs/cell), strong inhibitory effects were observed, with CXCL10 expression reduced to ≤ 0.126 (NB) and 0.248 (B), and CCL2 reduced to ≤ 0.094 (NB) and 0.118 (B). These data highlight the potent gene-modulatory capacity of both EV preparations, even at lower concentrations. Notably, NB-derived Av-EVs consistently outperformed the B-derived Av-EVs across all doses for both gene targets, with a statistically significant difference at the lowest dose for CXCL10 expression.

In addition, the pro-inflammatory cytokines IL-1β and TNF-α were also evaluated. IL-1β is a canonical early-response cytokine, tightly linked to inflammasome activation, and is a major driver of tissue inflammation and fibrosis. TNF-α, a central cytokine in M1-driven inflammation, initiates and sustains pro-inflammatory cascades in response to endotoxins like LPS. As expected, both IL-1β and TNF-α were significantly upregulated in LPS-stimulated macrophages. Upon cotreatment with Av-EVs, both cytokines were strongly downregulated across all doses, with D3 (5000 EVs/cell) achieving the maximum suppression, regardless of the extraction method. Previous research in Aloe vera-EVs also demonstrated this dose-dependent effect.[35, 36] Interestingly, at lower and intermediate doses (D1 and D2), B Av-EVs exhibited superior suppressive effects compared to NB, with D2 (2500 EVs/cell) demonstrating comparable efficacy to D3 in both preparations.

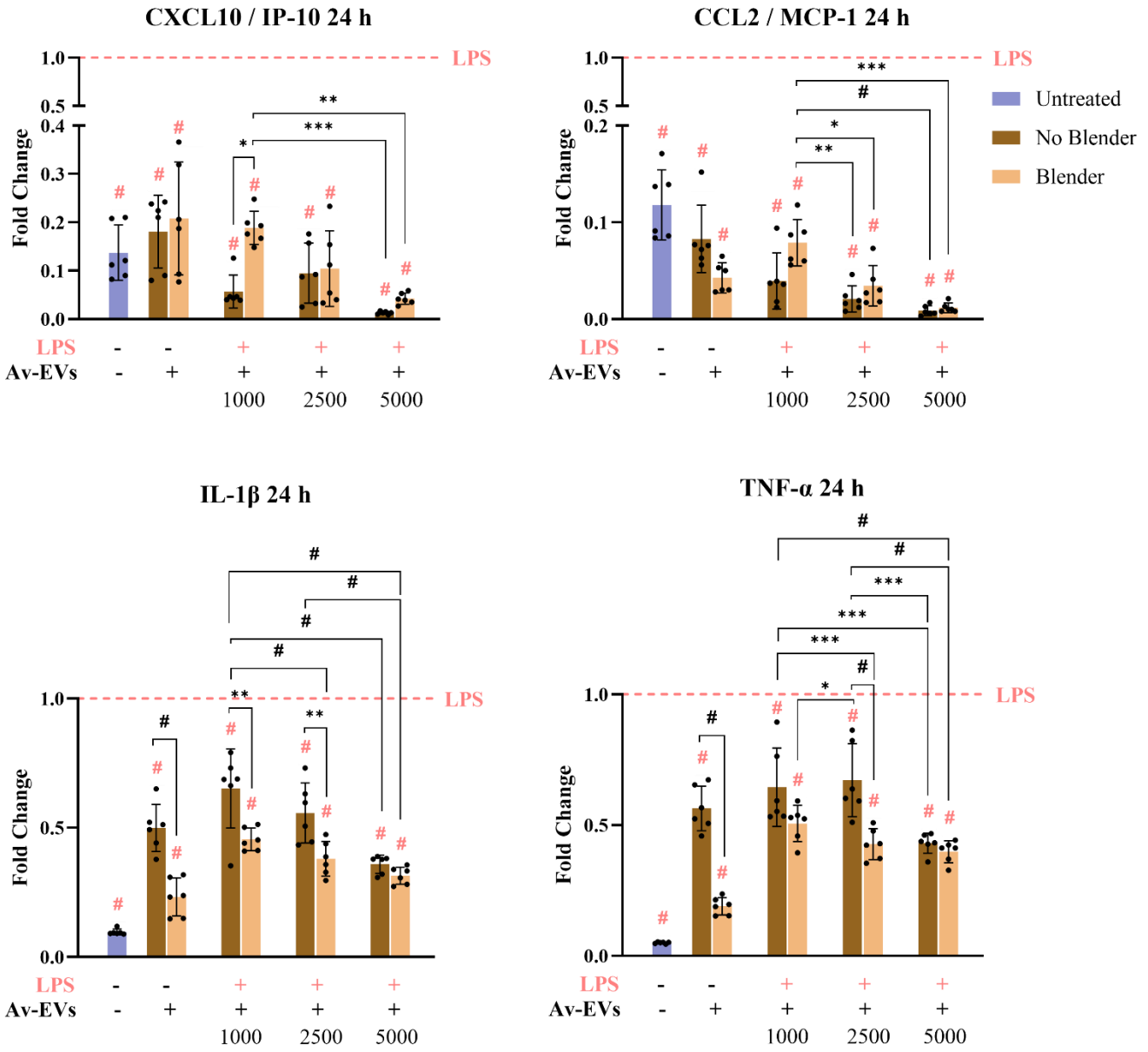

Figure 6. *CXCL10/IP-10, CCL2/MCP-1, IL-1β, TNF-α gene expressions in LPS-induced macrophages after 24 h of co-treatment with No Blender or Blender Av-EVs at increasing doses (1,000, 2,500, 5,000 EVs/cell). RT-qPCR data represents the mean ± SD with n=6 and p < 0.05 *, < 0.01 **, < 0.001 ***, < 0.0001 #. Statistical differences relative to the inflammatory control (+LPS/-EVs) are shown in pink, while statistical differences between the isolation methods and doses are shown in black.*

The observed suppression of these cytokines following Av-EV treatment demonstrates that Av-EVs act rapidly and effectively to modulate macrophage inflammatory responses. Upon LPS stimulation, Toll-like receptor 4 (TLR4) activation triggers the MyD88-dependent signaling cascade, leading to phosphorylation and degradation of IκBα, which permits nuclear translocation of NF-κB p65/p50 dimers and subsequent transcription of a wide array of pro-inflammatory genes, including CXCL10, CCL2, IL-1β, TNF-α, and IL-6. The downregulation of IL-1β and TNF-α, in particular, implies that Av-EVs could interfere with canonical TLR4/NF-κB signaling, potentially by inhibiting upstream kinases such as IKK, preserving IκBα stability, and ultimately preventing NF-κB nuclear localization.[55] This inhibitory effect may be attributed to specific phytochemical compounds within Av-EVs –such as flavonoids and miRNAs– previously shown to antagonize NF-κB signaling and inflammatory gene expression.[56-58] However, given the complexity of LPS-induced signaling, which also activates parallel inflammatory cascades such as the MAPK (ERK, JNK, p38) and PI3K/AKT pathways, further studies are warranted to elucidate the broader molecular mechanisms by which Av-EVs exert their immunomodulatory effects.[55, 58]

Modulation of M1-to-M2 Polarization from 24 Hours to 7 Days

IL-6 is a pleiotropic cytokine with complex roles in both pro-inflammatory signaling and tissue regeneration, making its behavior during macrophage activation highly context-dependent. During the early phase of activation (24 hours), IL-6 was significantly upregulated in LPS-treated macrophages [**Figure 7**]. At this point, Av-EV treatment did not result in a substantial modulation of IL-6 expression, regardless of dose or isolation method. This suggests that IL-6 expression during the acute inflammatory response is initially resistant to Av-EV-mediated suppression. After 72 hours, a notable shift occurred. IL-6 expression was significantly downregulated in Av-EV-treated groups compared to the LPS-only condition, with p-values reaching < 0.001 and < 0.0001 at intermediate and high doses for both NB and B EVs. This delayed suppression aligns with the early resolution phase of inflammation, during which IL-6 transitions from a pro-inflammatory effector to a mediator of immune regulation and repair and confirming that IL-6 elevation was part of a controlled resolution process rather than chronic inflammation.

Importantly, IL-6 appeared to play a transitional role in initiating macrophage phenotype switching from M1 to M2, a process supported by the concurrent rise in IL-10 expression.[59-62] This pattern is consistent with the activation of STAT3-mediated signaling as described in the literature, where both IL-6 and IL-10 are known to engage the Janus kinase (JAK)/signal transducer and activator of transcription 3 (STAT3) pathway. Upon receptor engagement, these cytokines trigger JAK phosphorylation, which subsequently activates STAT3 through tyrosine phosphorylation. Activated STAT3 then dimerizes and translocates into the nucleus, promoting transcription of anti-inflammatory and reparative genes such as SOCS3, ARG1, and IL-10.[61, 62] In the context of Av-EV treatment, the initial persistence of IL-6, followed by its suppression alongside peak IL-10 expression, suggests that Av-EVs may support a controlled, pro-resolving environment possibly involving STAT3 activity. While the current study did not directly assess STAT3 phosphorylation or nuclear translocation, the observed gene expression kinetics align with previously reported STAT3-dependent resolution mechanisms. By day 7, IL-6 remained consistently suppressed across all Av-EV-treated conditions, regardless of dose or extraction method, indicating the establishment of a stable, anti-inflammatory macrophage state, likely corresponding to M2 polarization and resolution of the inflammatory response.

In parallel, IL-10 expression patterns strongly support this interpretation. At 24 hours, both NB and B Av-EVs induced a dose-dependent upregulation of IL-10, with a particularly strong response at the lowest

dose (1000 EVs/cell) –inversely mirroring the IL-6 profile. Notably, NB EVs significantly outperformed B EVs in upregulating IL-10 at early and intermediate time points, suggesting superior early immunomodulatory potency. By 72 hours, IL-10 expression peaked in all EV-treated groups, coinciding with the sharp decline in IL-6 levels and further confirming the M1-to-M2 phenotypic transition. NB EVs again stood out, achieving up to a 5-fold increase in some replicates. By Day 7, IL-10 levels began to decline across all conditions, consistent with the transient nature of IL-10 in initiating the anti-inflammatory cascade and subsequent feedback mechanisms that restore immune homeostasis. This temporal profile underscores IL-10's role as an early switch that helps reset inflammatory macrophages toward a reparative fate –a transition likely sustained by STAT6-regulated downstream effectors such as ARG1 and IL-13, which appeared later in the timeline.[62]

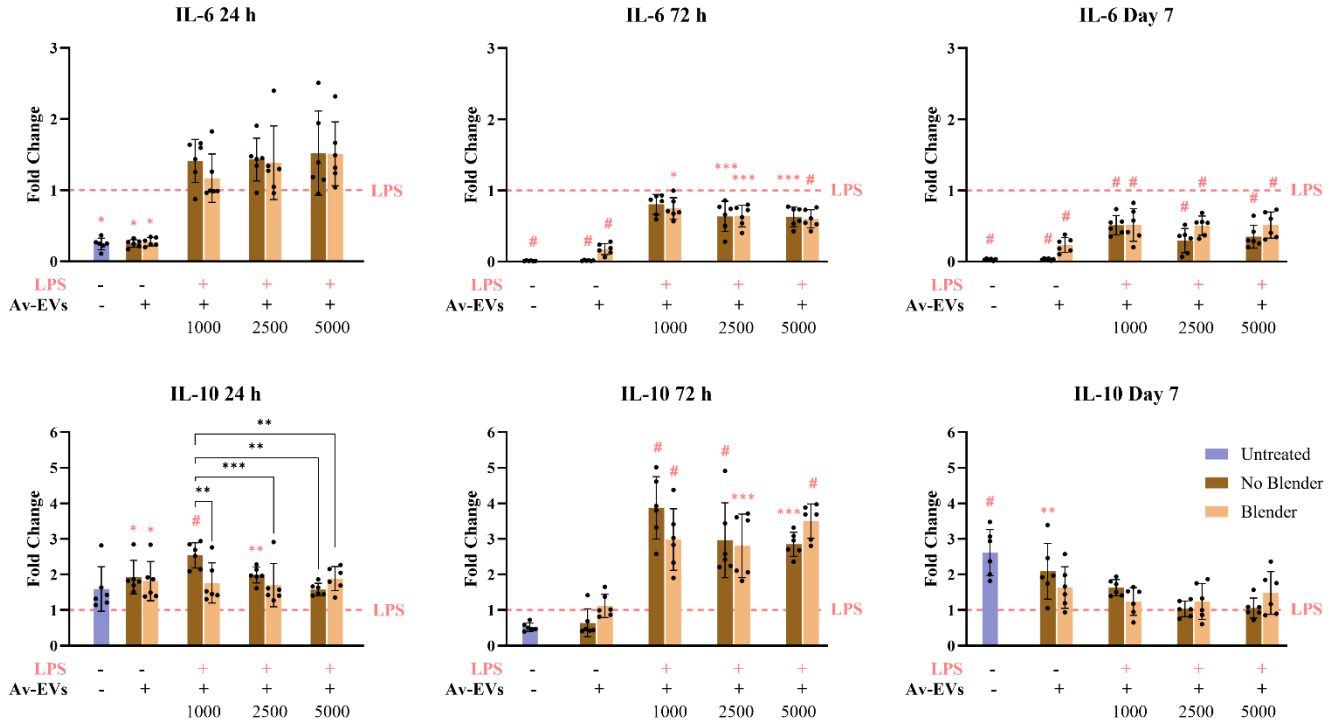

Figure 7. *IL-6 and IL-10 gene expressions in LPS-induced macrophages after 24 h, 72 h, and 7 days of co-treatment with No Blender or Blender Av-EVs at increasing doses (1,000, 2,500, 5,000 EVs/cell). RT-qPCR data represents the mean ± SD with n=6 and p < 0.05 *, < 0.01 **, < 0.001 ***, < 0.0001 #. Statistical differences relative to the inflammatory control (+LPS/-EVs) are shown in pink, while statistical differences between the isolation methods and doses are shown in black.*

Transition to an M2a Phenotype and Activation of Anti-inflammatory Markers in 7 Days

Although IL-10 expression declined by day 7, the sustained suppression of M1-associated cytokines – particularly during the critical 72-hour window – together with the concurrent upregulation of M2-associated markers, supports the notion of an orchestrated immune transition toward inflammation resolution and tissue repair. These findings suggest that Av-EV treatment facilitates a durable shift toward an anti-inflammatory phenotype, not only by mediating early immunosuppression but also by reinforcing late-stage macrophage reprogramming. In particular, the emergence of ARG1 and IL-13 expression on day 7 [**Figure 8**], following the peak of IL-10 at 72 hours, implies a sequential transition from M2 to M2a polarization –a well-established immunological trajectory. While early M2 polarization is primarily driven by IL-10-induced STAT3 activation, the subsequent differentiation into the M2a subtype is regulated

through the STAT6 pathway, which triggered downstream of IL-4 and IL-13 receptor engagement and promotes the transcription of target genes such as ARG1 and IL-13 itself.[62-64] This transition is essential for initiating reparative processes such as wound healing, ECM remodeling, and fibrosis modulation, and reflects the maturation of macrophages into a specialized, tissue-repairing M2a state.

ARG1, a canonical M2a marker involved in proline synthesis and collagen stabilization,[63] was significantly upregulated in all Av-EV-treated groups compared to the LPS-only condition. While variability existed among replicates, several exhibited fold changes between 5 and 10, indicating a robust response. Although differences between EV doses and isolation methods did not reach statistical significance, a clear dose-dependent trend was observed in both types of EVs with a better response in NB Av-EVs with significance even at the lowest dose. The trend aligns with the alamarBlue viability data, where reduced metabolic activity at higher Av-EV concentrations on day 7 may reflect enhanced polarization toward a reparative, quiescent M2 phenotype, rather than cytotoxicity.

Similarly, IL-13, a Th2-associated cytokine that promotes collagen deposition, tissue remodeling, and inflammation resolution,[63, 65] was modestly induced in several Av-EV-treated replicates across all doses and EV types. Although statistical significance was not achieved, its expression – especially when considered alongside ARG1 upregulation – suggests that Av-EVs support not only a general M2 phenotype but actively promote the M2a maturation subtype. Notably, IL-13 expression was not detected at earlier time points (data not shown), reinforcing the idea that its induction reflects a later, more specialized phase of macrophage polarization. This transition represents a shift toward regenerative immune activity, rather than mere immunosuppression.

While M2a macrophages are known to facilitate tissue repair, under persistent inflammatory conditions they may contribute to pathological fibrosis through excessive collagen deposition.[66, 67] However, in this study, Av-EV treatment also resulted in significant downregulation of fibrotic markers COL1A1 and α-SMA in fibroblasts (see section 3.2.5), indicating that matrix remodeling occurred without promoting fibrotic tissue accumulation. Moreover, we have already demonstrated that Av-EVs strongly suppressed key pro-inflammatory mediators at earlier time points, suggesting that the inflammatory stimulus had been resolved. In this context, M2a macrophage activity likely operates under homeostatic regulation, supporting tissue regeneration while minimizing the risk of fibrosis.

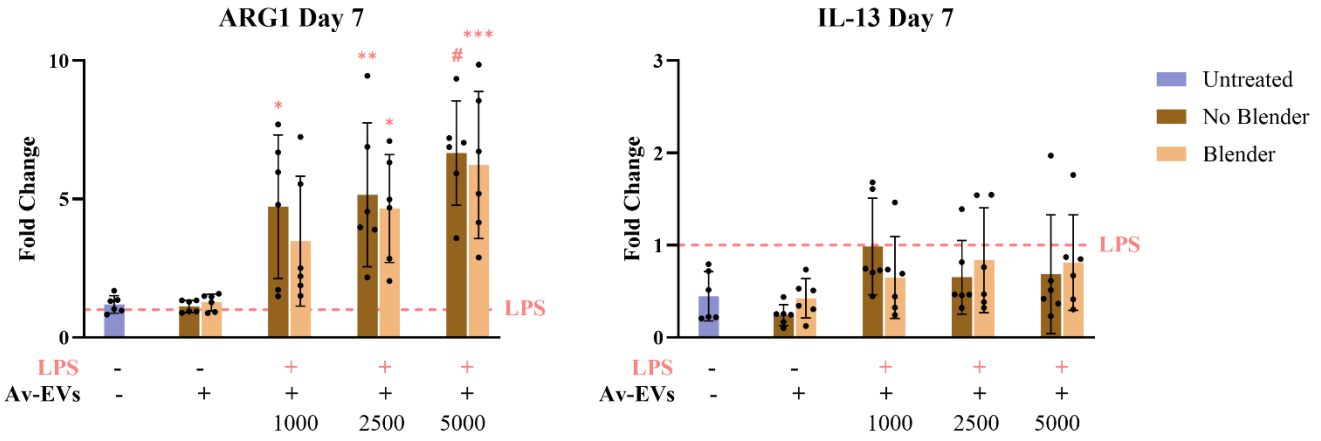

Figure 8. *ARG1 and IL-13 gene expressions in LPS-induced macrophages after 7 days of co-treatment with No Blender or Blender Av-EVs at increasing doses (1,000, 2,500, 5,000 EVs/cell). RT-qPCR data represents the mean ± SD with n=6 and p < 0.05 *, < 0.01 **, < 0.001 ***, < 0.0001 #. Statistical differences relative to the inflammatory control (+LPS/-EVs) are shown in pink.*

Taken together, these findings highlight the therapeutic potential of NB and B Av-EVs as naturally derived nanocarriers capable of orchestrating both early and late phases of macrophage reprogramming. By potentially guiding cells through a STAT3-associated anti-inflammatory state into a STAT6-driven tissue-regenerative phase, Av-EVs appear to promote scar matrix modulation and contribute to the resolution of pathological fibrosis – fully aligned with the study's overarching goal.

Interestingly, although IL-13 expression was successfully detected, attempts to quantify IL-4 expression by RT-qPCR yielded mostly in undetermined Ct values, suggesting very low or absent transcription under the tested conditions even by day 7 (data not shown). This raises the possibility that Av-EVs may activate the STAT6 pathway independently of IL-4, potentially through type II IL-4/IL-13 receptor complexes or IL-13 decoy receptor modulation – both of which are known to contribute to type 2 immune signaling and fibrotic regulation.[63-65] However, further research is necessary to elucidate the specific contributions of Av-EV cargo, including their RNA, lipid, and protein components, and how these may differentially modulate cytokine signaling, receptor engagement, and downstream transcriptional programming involved in M2 macrophage polarization and tissue remodeling.

3.2.5 Antifibrotic Response (Dermal Fibroblasts)

Myofibroblasts differentiation was induced in hDFs cultures exposed to 10 ng/mL TGF-β1, a potent pro-fibrotic factor that stimulates disorganized and excessive collagen deposition and enhances cell contractility and matrix tension by increasing the α-SMA stress fibers, mimicking the signaling observed in pathological scarring.[68] Additionally, vitamin C was used to enhance metabolic activity, growth and collagen production for a more robust fibrotic model.[69] Furthermore, the experiment investigated the potential of the three different doses of Av-EVs, isolated either manually or via shear force homogenization to attenuate this phenotype over a 72-hour exposure, by analyzing the gene expression of COL1A1 and α-SMA, two canonical myofibroblast markers. The experimental conditions were as stated in **Table 2**.

Figure 9 presents the fold change in gene expression for all treatment conditions relative to the fibrotic positive control (+TGF-β1+VitC/–EVs), which was normalized to a fold change of 1. This control group exhibited a marked upregulation in the expression of both genes compared to the untreated hDFs and the EV-only controls, aligning with the expected profile of excessive ECM deposition and myofibroblast accumulation characteristic of fibrotic states. In contrast, untreated hDFs showed COL1A1 expression levels ranging from 0.280 to 0.409, and α-SMA levels from 0.092 to 0.216, indicating a baseline, non-fibrotic state. Similarly, NB Av-EV controls exhibited fold change values between 0.282 – 0.420 for COL1A1 and 0.081 – 0.216 for α-SMA, while B Av-EV controls ranged from 0.180 – 0.424 for COL1A1 and 0.066 – 0.229 for α-SMA. These findings confirm that Av-EVs alone do not promote fibrotic activation in resting fibroblasts and maintain gene expression levels within a physiological range comparable to untreated cells.

The addition of Av-EVs attenuated TGF-β1/VitC-induced gene expression of both COL1A1 and α-SMA, indicating reduced myofibroblast differentiation. Despite the higher inter-replicate variability inherent to *in vitro* models with primary cells, NB-derived Av-EVs achieved the strongest downregulation at intermediate dose (2,500 EVs/cell), reaching p values of $p < 0.0001$ and $p < 0.001$ for COL1A1 and α-SMA, respectively, and a reduction of COL1A1 employing 5000 EVs/cell with a $p < 0.01$. Moreover, there was a statistically significant difference between NB and B Av-EVs at the same dose for COL1A1 with a $p < 0.01$, indicating that the manual method of isolation counteracts more effectively TGF-β1-

mediated transcriptional activation of collagen genes in comparison to those Av-EVs isolated via shear force homogenization.

These findings confirm the ability of Av-EVs to attenuate key markers of fibroblast-to-myofibroblast transdifferentiation and underscore their antifibrotic potential by inhibiting excessive ECM deposition and disrupting cytoskeletal reprogramming and mechanical force generation – both of which are critical for myofibroblast function and fibrotic scar contracture.[35, 54] This parallel reduction of COL1A1 and α-SMA implies that Av-EVs may interfere with TGF-β1/SMAD signaling pathways or their downstream effectors involved in fibrotic transformation. This hypothesis is supported by the well-characterized canonical TGF-β1 pathway, wherein ligand binding to its receptor complex (TGF-βRI/II) leads to phosphorylation of SMAD2 and SMAD3, which then form a transcriptionally active complex with SMAD4. This complex translocates to the nucleus to drive expression of pro-fibrotic genes such as COL1A1 and ACTA2 (α-SMA). Although direct inhibition of SMAD4 by Aloe vera components has not been demonstrated, several Aloe-derived bioactives, including acemannan, aloin and various flavonoids, have been shown to inhibit SMAD2/3 phosphorylation and nuclear translocation.[70, 71] This effectively disrupts the formation or function of the SMAD2/3/4 complex and impairs transcriptional activation of downstream fibrotic genes. Additionally, Aloe vera constituents may modulate non-canonical TGF-β pathways, such as ERK, p38 MAPK, RhoA/ROCK, and PI3K/AKT/mTOR, which further contribute to cytoskeletal remodeling and fibroblast activation and contractility.[21, 55, 72]

Taken together, these combined mechanisms strongly support the interpretation that the bioactive cargo of NB Av-EVs functions as a potent modulator of fibrotic signaling, effectively reprogramming fibroblasts away from a pro-fibrotic trajectory toward a more quiescent, regenerative phenotype. Furthermore, the dual activity of Av-EVs – immune modulation and fibroblast reprogramming – exert a coordinated regulation of inflammation and fibrosis, two key phases that must be tightly balanced to ensure effective wound healing and tissue regeneration without abnormal scar progression.

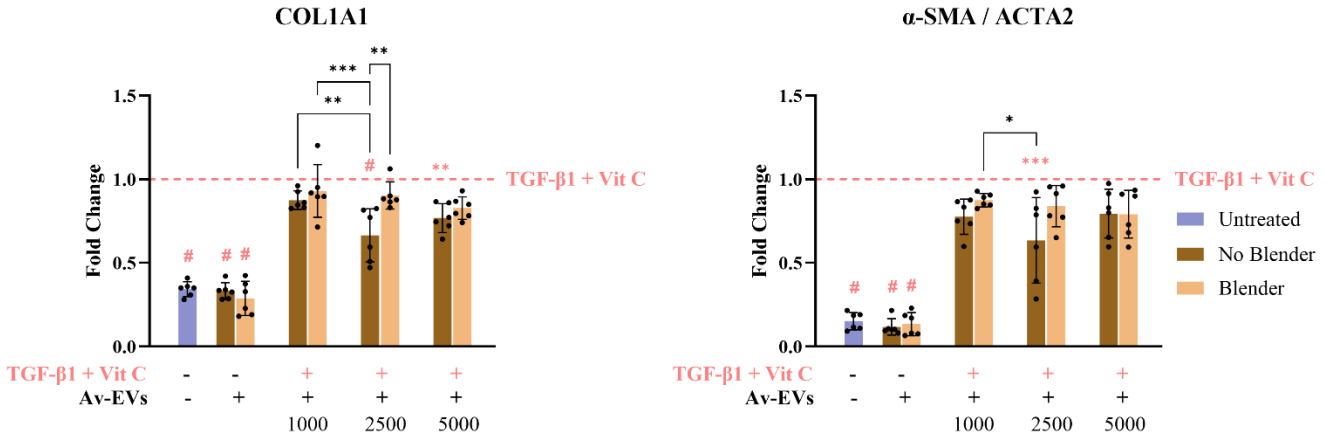

Figure 9. *COL1A1 and α-SMA/ACTA2 gene expressions in TGF-β1 + vitamin C- activated hDFs after 72 h co-treatment with No Blender or Blender Av-EVs at increasing doses (1,000, 2,500, 5,000 EVs/cell). RT-qPCR data represents the mean ± SD with n=6 and p < 0.05 *, < 0.01 **, < 0.001 ***, < 0.0001 #. relative to +TGFβ1+VitC/-EVs control. Statistical differences relative to the fibrotic control (+TGFβ1+VitC/-EVs) are shown in pink, while statistical differences between the isolation methods and doses are shown in black.*

3.2.6 Immunofluorescence Analysis of Smooth Muscle Actin

To further validate the antifibrotic properties of Av-EVs, α-SMA expression was assessed by immunofluorescence microscopy in hDFs cultured under healthy or fibrotic conditions, with or without

Av-EVs co-treatment (2,500 EVs/cell). α-SMA was labeled in green, F-actin in red, and cell nuclei in blue. For each condition, six α-SMA and six background pixel intensity measurements were collected from three independent images. Quantification was performed by calculating net α-SMA signal intensity as the difference between each α-SMA measurement and the average background value.

As shown in **Figure 10**, untreated hDFs (far left) exhibited a classic quiescent fibroblast morphology with elongated spindle-shaped cells with aligned F-actin filaments as seen in the cellular uptake analysis. Image analysis revealed low α-SMA intensity values (817.2 to 1,090.2) consistent with a non-activated state. In contrast, fibrotic control cells (second panel), treated with TGF-β1 and vitamin C, displayed extensive cytoskeletal remodeling and strong colocalization of α-SMA with F-actin, forming dense contractile stress fibers – a hallmark of activated myofibroblasts. Fluorescence intensity dramatically increased to 2,403.3 and 2,649.3, representing a 2.5- to 3-fold rise over untreated cells ($p < 0.0001$). These results align with those reported by Ramirez et al., who observed a fivefold increase in α-SMA expression in myofibroblasts relative to untreated fibroblasts.[35]

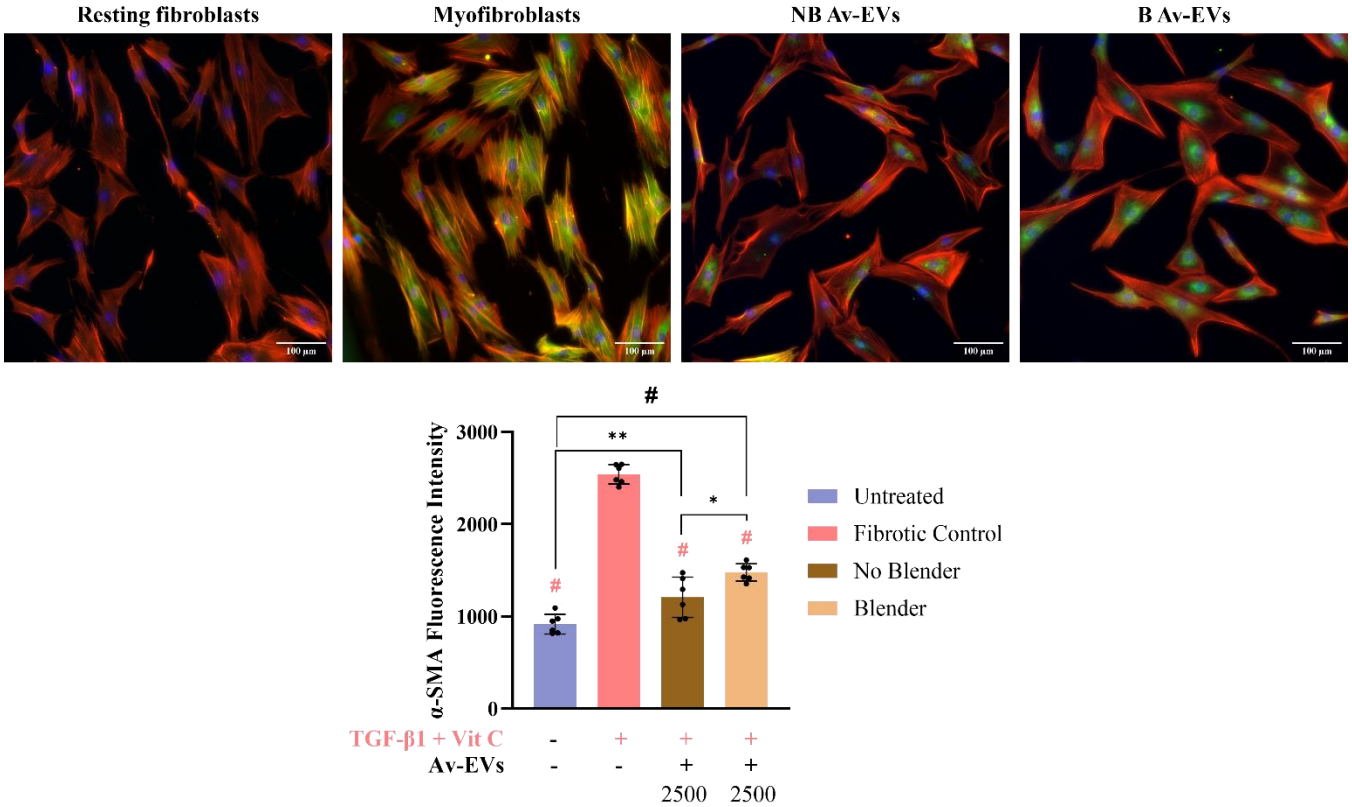

Figure 10. *Immunofluorescence staining of α-SMA (green), F-actin (red), and nuclei (blue) in hDFs. From left to right: resting hDFs, myofibroblast differentiation induced with TGF-β1 and vitamin C, and co-treatment with No Blender or Blender Av-EVs at 2,500 EVs/cell for 72 h. Images were captured at 20X magnification under identical exposure settings. α-SMA fluorescent intensity data represent mean ± SD with n=6 and p < 0.05 *, < 0.01 **, < 0.0001 #. Statistical differences relative to the fibrotic control (+TGFβ1+VitC/-EVs) are shown in pink, while statistical differences between the isolation methods are shown in black.*

Both Av-EV treatment groups significantly reduced α-SMA expression compared to the fibrotic control ($p < 0.0001$), with a significant difference between NB and B EVs ($p < 0.05$). NB Av-EV (third panel) reduced α-SMA levels to 966.8 – 1,474.8, effectively halving the fibrotic effect. Although the cells retained a spread morphology, they exhibited reduced colocalization and loss of organized stress fibers, suggesting diminished contractility and a shift toward a less fibrogenic state. B-derived EVs (fourth panel) also attenuated α-SMA expression (1,353.3 to 1,610.5), though less pronounced than NB-derived EVs.

Notably, when compared to untreated cells, NB EV-treated hDFs showed only a modest difference ($p < 0.01$), whereas B EV-treated cells maintained a stronger divergence ($p < 0.0001$), further underscoring the superior efficacy of NB vesicles in restoring α-SMA expression toward baseline.

These findings support the gene expression data and reinforce the conclusion that the manual isolation method better preserves the functional vesicle cargo responsible for modulating fibroblast activation. Moreover, they confirm that Av-EVs suppress TGF-β1- driven fibrotic cascade at both transcriptional and protein levels. By downregulating α-SMA and disrupting associated cytoskeletal remodeling, Av-EVs emerge as promising nanotherapeutic agents capable of reducing tissue stiffness, contracture, and pathological ECM deposition, offering potential in the prevention of hypertrophic scars and keloids.

3.3 Comparative Analysis of NB Av-EVs Isolated from Mature and Young Aloe vera Leaves

All results discussed thus far were obtained using EVs isolated – either manually or mechanically – from mature Aloe vera leaves sourced from a supermarket supplied by a large-scale distributor in the United States. These leaves exhibited consistent morphological characteristics (~67 cm × ~9 cm × ~3 cm) and yielded approximately 400 mL per leaf. Given their robust and reproducible performance in reducing pro-inflammatory and fibrotic markers – particularly for NB-derived EVs – we extended our investigation to assess EVs derived from young Aloe vera leaves, manually harvested from live potted plants obtained from a local plant shop. These younger leaves were notably smaller (~45 cm × ~5 cm × ~1.5 cm) and produced a reduced gel yield of ~100 mL per leaf. This comparative analysis between NB Av-EVs derived from mature and young Aloe vera leaves is not only scientifically relevant but also holds important translational implications. Since Aloe vera plants require several years to reach full maturity – a factor that directly affects cultivation time, production scalability, and manufacturing costs –, understanding whether younger plants can yield vesicles with comparable therapeutic efficacy is critical for future commercialization efforts. Evaluating how plant age and extraction method influence EV composition and bioactivity may help streamline production strategies and inform selection criteria for cost-effective, large-scale Av-EV manufacturing.

3.3.1 Anti-Inflammatory Response (Macrophages)

Co-treatment with Av-EVs from both mature and young leaves resulted in attenuation of M1-associated pro-inflammatory cytokines (CXCL10/IP-10, CCL2/MCP-1, IL-1β, TNF, IL-6); however, mature leaf-derived EVs consistently outperformed young EVs across all measured markers [**Figure 11**]. Please note that separate untreated controls were included for the mature and young Aloe vera EV groups, as these samples were processed and analyzed in independent experimental runs.

CXCL10 and CCL2 were significantly downregulated by both EV types in a dose-dependent manner. Yet, NB-mature EVs achieved near-complete suppression at the lowest dose, while young EVs required the highest dose to reach comparable levels, highlighting a marked difference in potency. A significant difference ($p < 0.001$ for CXCL10; $p < 0.0001$ for CCL2) was observed between the two groups at the lowest dose. Furthermore, basal levels of these chemokines were elevated in young EV-only controls in comparison with the mature EV-only controls, with CCL2 showing statistical significance ($p < 0.01$), suggesting inherent differences in vesicle content or cell responsiveness.

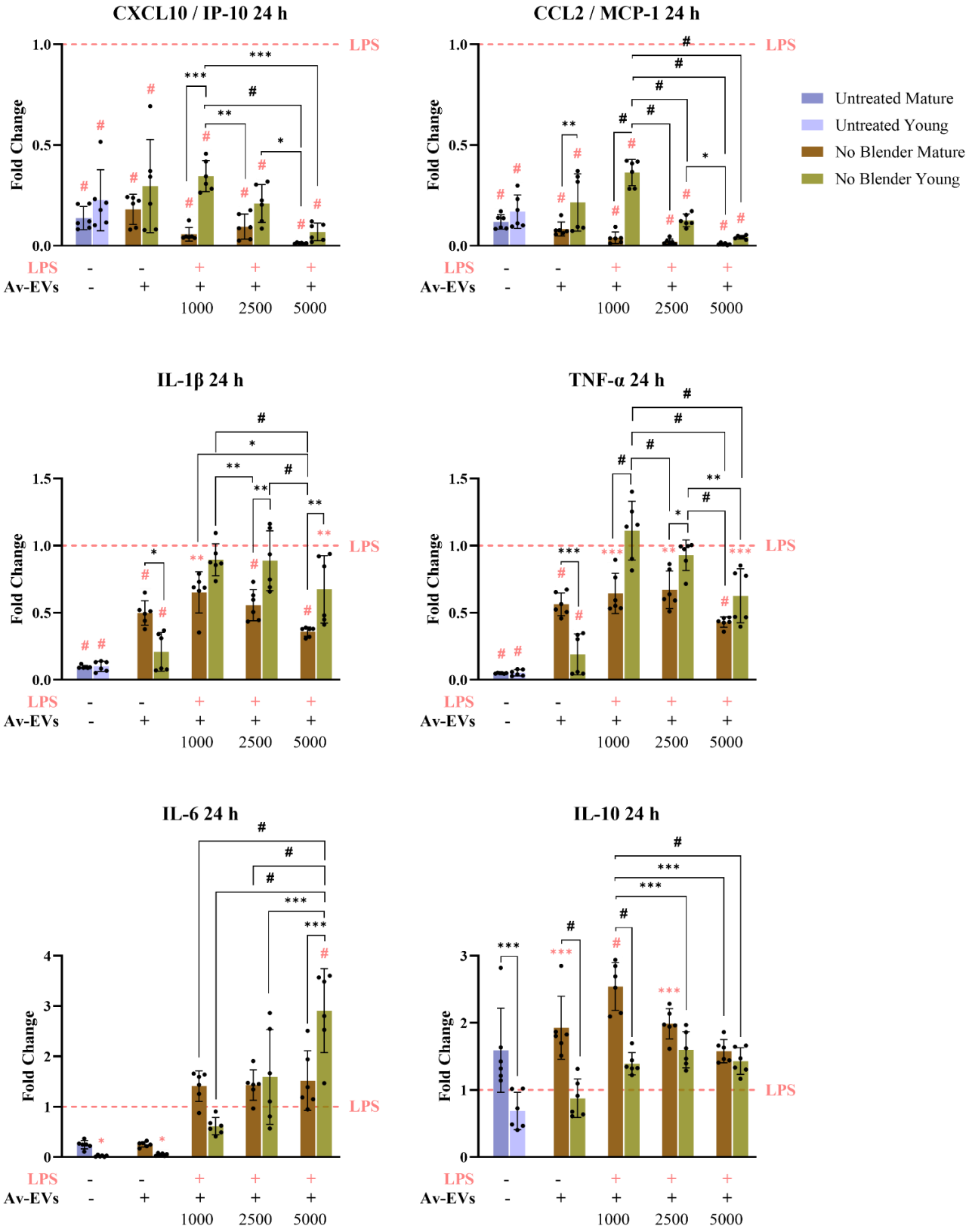

Figure 11. *CXCL10/IP-10, CCL2/MCP-1, IL-1β, TNF-α, IL-6 and IL-10 gene expressions in LPS-induced macrophages after 24 h of co-treatment with No Blender Av-EVs (isolated from mature or young Aloe vera leaves) at increasing doses (1,000, 2,500, 5,000 EVs/cell). RT-qPCR data represents the mean ± SD with n=6 and p value < 0.05 *, < 0.01 **, < 0.001 ***, < 0.0001 #. Statistical differences relative to the inflammatory control (+LPS/-EVs) are shown in pink, while statistical differences between the plant maturity and doses are shown in black.*

While IL-1β and TNF-α exhibited modest, dose-dependent downregulation in response to young EVs, their suppression remained consistently inferior to that achieved with mature EVs – with even the lowest dose of mature EVs outperforming the highest dose of young counterparts. Statistically significant differences between the two groups were evident across multiple doses, including $p < 0.01$ at D2 and D3 for IL-1β, and $p < 0.0001$ at D1 and $p < 0.05$ at D2 for TNF-α, underscoring the limited anti-inflammatory efficacy of young EVs. Interestingly, and unlike the trends observed for CXCL10 and CCL2, both IL-1β and TNF-α were significantly lower in the young EV-only control groups compared to the mature EV control groups, reaching $p < 0.05$ for IL-1β and $p < 0.001$ for TNF-α. This suggests different immune responses by vesicles from plants at different stages of development. Nevertheless, young EVs were unable to restore cytokine expression to baseline levels in the treated cells, in contrast to the superior immunomodulatory capacity of mature EVs.

Surprisingly, IL-6 expression exhibited a clear dose-dependent increase in cells treated with young Av-EVs, reaching fold changes of up to 4 at the highest concentration. This response stands in contrast to the stable IL-6 expression observed in mature EV-treated groups, resulting in a statistically significant difference between the highest dose groups ($p < 0.001$). These findings suggest that young EVs may not only lack the capacity to suppress IL-6-mediated inflammatory signaling, but at elevated doses, may in fact intensify the inflammatory response, highlighting a potential pro-inflammatory liability associated with immature vesicle cargo. In parallel, IL-10 expression was only modestly elevated in cells treated with young Av-EVs, displaying no clear dose-dependent trend and no significant difference from the LPS-only group, in contrast to mature Av-EVs, where induced IL-10 expression was in a consistent, dose-responsive manner opposite to IL-6 profile, with the most pronounced effect observed at the lowest dose, where expression was significantly higher than in the young EV group ($p < 0.0001$). Moreover, IL-10 levels in the young EV-only control group were markedly lower than those in the mature EV-only control ($p < 0.0001$), suggesting that the baseline immunomodulatory potential of vesicles from immature plants may be intrinsically limited.

3.3.2 Antifibrotic Response (Dermal Fibroblasts)

When evaluating fibrotic gene expressions (COL1A1 and α-SMA), young EVs again failed to match the efficacy of mature EVs [**Figure 12**]. Please note that separate untreated controls were included for the mature and young Aloe vera EV groups, as these samples were processed and analyzed in independent experimental runs.

Although a weak dose-response trend was observed, even the highest dose of young EVs did not reduce expression below that achieved by the lowest dose of mature EVs in any of the two targets. For COL1A1, significant differences were observed across all doses between the types of EVs ($p < 0.0001$ at D1 and D2; $p < 0.01$ at D3), and similar patterns were evident for α-SMA ($p < 0.001$ at D1 and $p < 0.0001$ at D2). These results highlight the superior antifibrotic potential of mature Av-EVs, which are more effective in preventing fibroblast-to-myofibroblast transdifferentiation, a key process in pathological scar formation.

Collectively, the results clearly highlight that EVs derived from mature Aloe vera leaves possess markedly superior anti-inflammatory and antifibrotic properties compared to those from younger plants. Mature Av-EVs consistently outperformed their younger counterparts, achieving stronger downregulation of inflammatory mediators and fibrotic markers, and demonstrating enhanced IL-10 upregulation. In contrast, young Av-EVs not only exhibited limited efficacy, but in some cases induced paradoxical pro-inflammatory effects, such as increased IL-6 expression at higher doses. These findings align with

previous work on orange-derived EVs, where the maturity of the fruit significantly influenced vesicle characteristics, including particle concentration and diameter, surface potential, lipid and protein content, and their ability to encapsulate and deliver bioactive compounds. Specifically, vesicles from ripe orange juice demonstrated superior curcumin delivery performance – enhancing its solubility, stability, bioaccessibility, and antioxidant activity – compared to those from unripe or overripe sources.[73] Given curcumin's well-established anti-inflammatory properties, this further supports the concept that plant maturity plays a crucial role in optimizing the therapeutic potential of EV-based delivery systems.

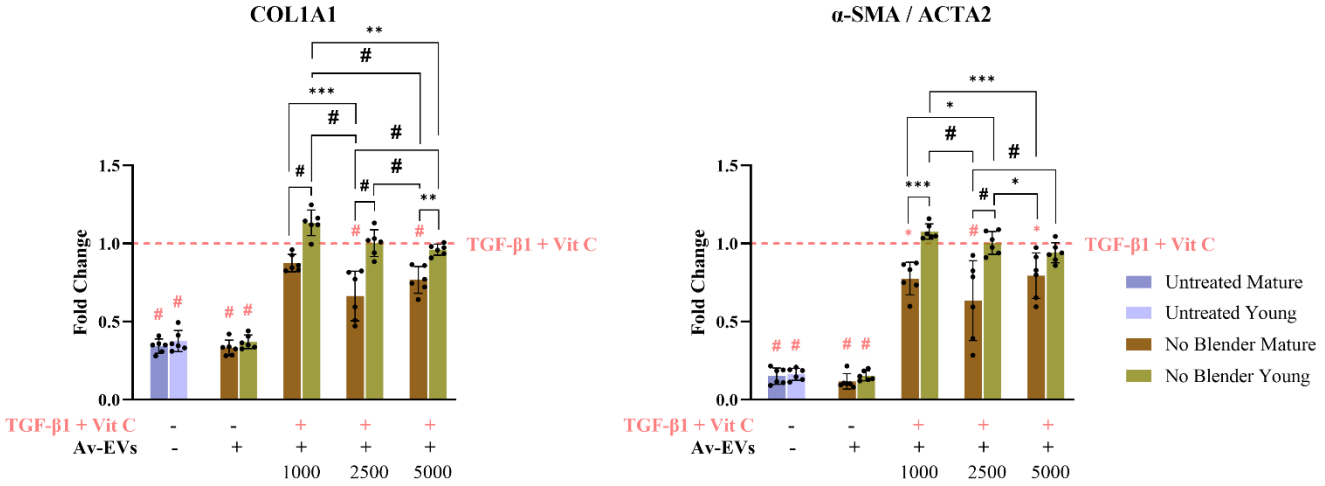

Figure 12. *COL1A1 and α-SMA/ACTA2 gene expressions in TGF-β1 + vitamin C- activated hDFs after 72 h co-treatment with No Blender Av-EVs (isolated from mature or young Aloe vera leaves) at increasing doses (1,000, 2,500, 5,000 EVs/cell). RT-qPCR data represents the mean ± SD with n=6 and p value < 0.05 *, < 0.01 **, < 0.001 ***, < 0.0001 #. Statistical differences relative to the fibrotic control (+TGFβ1+VitC/-EVs) are shown in pink, while statistical differences between the plant maturity and doses are shown in black.*

3.3.3 Biological Considerations: Av-EVs from Mature versus Young Aloe vera Leaves

The disparity in the anti-inflammatory and antifibrotic efficacy observed between mature and young Av-EVs is likely rooted in biological differences in vesicle cargo and surface marker profiles, which are inherently influenced by the plant's age, developmental stage, and growing conditions.[74] Mature leaves from supermarket-grade Aloe vera *barbadensis miller* plants are typically cultivated under controlled agronomic environments optimized for commercial use. These conditions favor the accumulation of polysaccharides (e.g., acemannan), sterols, flavonoids, and other secondary metabolites that are well-documented for their anti-inflammatory, antioxidant, and immunomodulatory properties.[75, 76] In contrast, younger nursery-grown plants, especially those intended for ornamental purposes, are less metabolically mature. Their smaller biomass, lower gel yield, and underdeveloped biosynthetic pathways likely contribute to a less complex and less bioactive EV cargo. This includes potential deficits in regulatory lipids, miRNAs, and proteins involved in modulating key inflammatory and fibrotic signaling cascades such as NF-κB and STAT3/STAT6 in macrophages, and TGF-β1/SMAD in fibroblasts. These molecular deficiencies may explain the reduced potency of young Av-EVs in downregulating pro-inflammatory cytokines or reversing myofibroblast-associated gene expression.

These findings highlight the critical role of plant maturity, cultivation purpose, and bioactive composition in determining the therapeutic potential of Aloe-derived bioproducts. In particular, the biochemical and functional properties of Av-EVs can vary substantially depending on factors such as Aloe species, plant age, geographical origin, climate, soil type, and extraction methodology.[77-79] Importantly, the optimal

harvest time for Aloe leaves is typically after three years of growth, when bioactive compound content peaks.[75] Furthermore, post-harvest handling, storage, and transport conditions play a pivotal role in preserving bioactivity, since exposure to excessive light, heat, or humidity can degrade key molecules before vesicle isolation.[30, 75, 77, 79]

To address these limitations, the variables mentioned must be carefully controlled to ensure the reproducibility and potency of EV-based therapeutics derived from Aloe plant sources. Future research should prioritize the identification of lead compounds within Av-EVs that are responsible for their therapeutic effects. To this end, we plan to conduct a comprehensive multiomics analysis – including proteomics, small RNA sequencing, and metabolomics – to characterize and compare the molecular cargo of EVs derived from mature versus young Aloe vera leaves. This approach will help identify biologically active components that may underline the observed differences in bioactivity and support the rational selection of lead candidates. Ultimately, these insights will facilitate the development of standardized protein or multi-component formulations that retain therapeutic efficacy independent of plant variability, streamlining both clinical translation and regulatory approval.

4. Conclusion

In this study, extracellular vesicles derived from Aloe vera gel (Av-EVs) were successfully isolated using either manual (NB) or shear-force-based (B) extraction methods and comprehensively characterized in accordance with MISEV2023 guidelines. The vesicles exhibited expected spherical morphology, size distribution of 150 – 250 nm, and consistent yields of 5.6 to 8×10^{11} particles per mature leaf, establishing a robust foundation for downstream *in vitro* functional assays. Notably, differences in particle concentration and protein content between NB and B samples underscored the critical influence of extraction methodology on vesicle integrity and potential bioactivity.

The antioxidant activity of Av-EVs, assessed via DPPH radical scavenging, revealed strong time-dependent inhibition of oxidative markers. NB-derived vesicles consistently outperformed B-derived counterparts, particularly at intermediate and high concentrations, suggesting that gentle extraction may have an advantage in retaining redox-active components. These antioxidant effects are relevant given their overlap with non-cytotoxic concentrations effective in subsequent anti-inflammatory and antifibrotic assays. As excessive ROS perpetuates inflammation and fibrosis through pathways like TGF-β1/NOX4, the ability of Av-EVs to neutralize free radicals *in vitro* supports their potential role in breaking the oxidative stress–fibrosis cycle and restoring tissue homeostasis during wound repair.

Cytocompatibility was confirmed in both THP-1-derived macrophages and human dermal fibroblasts (hDFs), where Av-EVs preserved cell viability while facilitating downstream phenotypic modulation. Fluorescence imaging further validated their intracellular uptake without compromising cytoskeletal structure, reinforcing their suitability as bioactive nanocarriers.

Functionally, both NB and B Av-EVs demonstrated potent immunomodulatory activity in an *in vitro* model of LPS-induced macrophage polarization. A rapid and sustained downregulation of M1-associated cytokines (CXCL10, CCL2, IL-1β, TNF-α, IL-6) was observed within 24 hours of treatment, followed by IL-10 upregulation and IL-6 suppression at 72 hours. By day 7, increased expression of M2a markers (Arg1, IL-13) indicated a sequential and durable shift from pro-inflammatory M1 to pro-resolving

M2/M2a phenotypes. These transitions suggest that Av-EVs likely engage key signaling pathways such as suppression of NF-κB and potential activation of STAT3/STAT6, indicating a coordinated reprogramming of macrophage function toward inflammation resolution and tissue repair.

In parallel, Av-EVs significantly attenuated myofibroblasts differentiation *in vitro*, a hallmark of fibrotic progression. NB-derived vesicles, particularly at intermediate and high doses, effectively downregulated COL1A1 and α-SMA gene expression. Immunofluorescence analysis confirmed a significant drop in α-SMA signal intensity and reduced stress fiber formation, indicating suppression of the contractile, fibrogenic phenotype in both groups; however, there was a difference of $p < 0.05$ in favor of NB EVs. The differential efficacy between NB and B EVs across cell types (THP-1-derived macrophages and hDFs) may reflect differences in cargo preservation and downstream signaling engagement, emphasizing the importance of tailoring isolation protocols to specific therapeutic goals. It is also worth noting that the observed biological effects may be influenced not only by the vesicle-intrinsic content but also by co-isolated biomolecules or vesicle-like particles present in the final suspension, which could contribute additively or synergistically to the functional outcomes in each assay.

Importantly, vesicles manually isolated (NB) from mature Aloe vera leaves consistently outperformed those from younger plants in both anti-inflammatory and antifibrotic assays. These findings highlight the influence of plant maturity, physiological state, and cultivation conditions on EV composition and reinforce the need for standardization in raw material sourcing for plant-derived nanotherapeutics and the identification of lead compounds within Av-EVs that are responsible for their therapeutic effects.

Taken together, this work establishes Av-EVs – particularly those manually extracted from mature Aloe vera leaves – as promising multifunctional candidates capable of attenuating oxidative stress and fibroblast activation and differentiation, and promoting pro-repair immune responses, *in vitro*. By targeting key interconnected drivers of abnormal wound healing and fibrosis, Av-EVs represent a scalable and biocompatible platform with high translation potential. Further investigations should focus on detailed cargo profiling using multi-omics approaches (e.g., proteins, miRNAs, and metabolites), mechanistic mapping of signaling pathways (e.g., NF-κB, STAT3, STAT6), and evaluation in relevant *in vivo* wound healing and fibrosis models. Additionally, incorporation into delivery systems such as dissolvable microneedle patches could enhance targeted application and patient compliance. While the present findings are limited to *in vitro* contexts, they provide a foundation for the preclinical development of Av-EVs as natural, cell-free nanotherapeutics for scar modulation and regenerative medicine.

Acknowledgments

The authors gratefully acknowledge the members of the Abhyankar Lab Biological Microsystems at Rochester Institute of Technology for their technical assistance with fluorescence microscopy, especially Ph.D. candidates Poorya Esmailis and Indranil "Neil" Joshi.

Conflicts of interest

The authors declare no conflict of interest.

References

1. Xue, M. and C. Jackson, *Extracellular Matrix Reorganization During Wound Healing and Its Impact on Abnormal Scarring.* Advances in Wound Care, 2015. **4**(3): p. 119-136.
2. Shroff, A., A. Mamalis, and J. Jagdeo, *Oxidative Stress and Skin Fibrosis.* Current Pathobiology Reports, 2014. **2**(4): p. 257-267.
3. Mittal, M., et al., *Reactive Oxygen Species in Inflammation and Tissue Injury.* Antioxid Redox Signaling, 2014. **20**(7): p. 1126-1167.
4. Antar, S., et al., *Fibrosis: Types, Effects, Markers, Mechanisms for Disease Progression, and Its Relation with Oxidative Stress, Immunity, and Inflammation.* International Journal of Moleculas Sciences, 2023. **24**(4): p. 4004.
5. Piera-Velasquez, S. and S.A. Jimenez, *Oxidative Stress Induced by Reactive Oxygen Species (ROS) and NADPH Oxidase 4 (NOX4) in the Pathogenesis of the Fibrotic Process in Systemic Sclerosis: A Promising Therapeutic Target.* Journal of Clinical Medicine, 2021. **10**(20): p. 4791.
6. Kumar, R., et al., *Therapeutic potential of Aloe vera—A miracle gift of nature.* Phytomedicine, 2019. **60**: p. 152996.
7. Sánchez-Machado, D., et al., *Aloe vera: Ancient knowledge with new frontiers.* Trends in Food Science & Technology, 2017. **61**: p. 94-102.
8. Radha, M.H. and N.P. Laxmipriya, *Evaluation of biological properties and clinical effectiveness of Aloe vera: A systematic review.* Journal of Traditional and Complementary Medicine, 2015. **5**(1): p. 21-26.
9. Pereira, R., et al., *Development of novel alginate based hydrogel films for wound healing applications.* International Journal of Biological Macromolecules, 2013. **52**: p. 221-230.
10. Sánchez, M., et al., *Pharmacological Update Properties of Aloe Vera and its Major Active Constituents.* Molecules, 2020. **25**(6): p. 1324.
11. Hamman, J.H., *Composition and Applications of Aloe vera Leaf Gel.* Molecules, 2008. **13**(8): p. 1599-1616.
12. Alawad, W., et al., *Effect of aloe vera hydrogel on the scarring and healing of free gingival graft: Randomized controlled trial.* Dentistry 3000, 2022. **10**(1).
13. Zhang, N., et al., *Modulating cationicity of chitosan hydrogel to prevent hypertrophic scar formation during wound healing.* International Journal of Biological Macromolecules, 2020. **154**: p. 835-843.
14. Danish, P., et al., *Antifungal and Antibacterial Activity of Aloe vera Plant Extract.* Biological and Clinical Sciences Research Journal, 2020. **4**.
15. Hekmatpou, D., et al., *The Effect of Aloe Vera Clinical Trials on Prevention and Healing of Skin Wound: A Systematic Review.* Iranian Journal of Medical Sciences, 2019. **44**(1): p. 1-9.
16. Singh, S., A. Gupta, and B. Gupta, *Scar free healing mediated by the release of aloe vera and manuka honey from dextran bionanocomposite wound dressings.* International Journal of Biological Macromolecules, 2018. **120**: p. 1581-1590.
17. Hormozi, M., R. Assaei, and M.B. Boroujeni, *The effect of aloe vera on the expression of wound healing factors (TGFβ1 and bFGF) in mouse embryonic fibroblast cell: In vitro study.* Biomedicine & Pharmacotherapy, 2017. **88**: p. 610-616.
18. Oryan, A., et al., *Topical Application of Aloe vera Accelerated Wound Healing, Modeling, and Remodeling.* Annals of Plastic Surgery, 2016. **77**(1): p. 37-46.
19. Avijgan, M., A. Kamran, and A. Abedini, *Effectiveness of Aloe Vera Gel in Chronic Ulcers in Comparison with Conventional Treatments.* Iranian Journal of Medical Sciences, 2016. **41**.
20. Eghdampour, F., et al., *The Impact of Aloe vera and Calendula on Perineal Healing after Episiotomy in Primiparous Women: A Randomized Clinical Trial.* Journal of Caring Sciences, 2013. **2**(4): p. 279-286.

21. Budai, M.M., et al., *Aloe vera downregulates LPS-induced inflammatory cytokine production and expression of NLRP3 inflammasome in human macrophages.* 2013(56): p. 471-479.
22. Nejatzadeh-Barandozi, F., *Antibacterial activities and antioxidant capacity of Aloe vera.* Organic and Medical Chemistry Letters, 2013. **3**(5).
23. Saini, D., Saini, M., *Evaluation of radioprotective efficacy and possible mechanism of action of Aloe gel.* Environmental Toxicology and Pharmacology, 2011. **31**(3): p. 427-435.
24. Yun, N., C.-H. Lee, and S.M. Lee, *Protective effect of Aloe vera on polymicrobial sepsis in mice.* Food and Chemical Toxicology. **47**: p. 1341-1348.
25. Habeeb, F., et al., *The inner gel component of Aloe vera suppresses bacterial-induced pro-inflammatory cytokines from human immune cells.* Methods, 2007. **42**(4): p. 388-393.
26. Eamlamnam, K., et al., *Effects of Aloe vera and sucralfate on gastric microcirculatory changes, cytokine levels and gastric ulcer healing in rats.* World Journal of Gastroenterology, 2006. **12**(13): p. 2034-2039.
27. Prabjone, R., et al., *Anti-inflammatory effects of Aloe vera on leukocyte–endothelium interaction in the gastric microcirculation of Helicobacter pylori-infected rats.* Clinical Hemorheology and Microcirculation, 2006. **35**(3): p. 359-366.
28. Langmead, R.J. and D.S. Makins, *Anti-inflammatory effects of aloe vera gel in human colorectal mucosa in vitro.* Alimentary Pharmacology and Therapeutics, 2004. **19**(5): p. 521-527.
29. Woo, S.W., et al., *Aloe Emodin Suppresses Myofibroblastic Differentiation of Rat Hepatic Stellate Cells in Primary Culture.* Pharmacology & Toxicology, 2002. **90**(4): p. 193-198.
30. Alzahrani, F.A., et al., *Plant-Derived Extracellular Vesicles and Their Exciting Potential as the Future of Next-Generation Drug Delivery.* Biomolecules, 2023. **13**(5): p. 839.
31. Kim, M., et al., *Therapeutic Applications of Plant-Derived Extracellular Vesicles as Antioxidants for Oxidative Stress-Related Diseases.* Antioxidants, 2023. **12**(6): p. 1286.
32. Liu, X., Lou, K., Zhang, Y., Li, C., Wei, S., Feng, S., *Unlocking the Medicinal Potential of Plant-Derived Extracellular Vesicles: current Progress and Future Perspectives.* International Journal of Nanomedicine, 2024. **19**: p. 4877-4892.
33. Calzoni, E., Bertoldi, A., Cusumano, G., Buratta, S., Urbanelli, L., Emiliani, C., *Plant-Derived Extracellular Vesicles: Natural Nanocarriers for Biotechnological Drugs.* Processes, 2024. **12**(12): p. 2938.
34. Bahmani, L., Ullah, M., *Different Sourced Extracellular Vesicles and Their Potential Applications in Clinical Treatments.* Cells, 2022. **11**(13): p. 1989.
35. Ramírez, O., et al., *Aloe vera peel-derived nanovesicles display anti-inflammatory properties and prevent myofibroblast differentiation.* Phytomedicine, 2024. **122**: p. 155108.
36. Kim, M. and J.H. Park, *Isolation of Aloe saponaria-Derived Extracellular Vesicles and Investigation of Their Potential for Chronic Wound Healing.* Pharmaceutics, 2022. **14**: p. 1905.
37. Kim, M.K., et al., *The Antioxidant Effect of Small Extracellular Vesicles Derived from Aloe vera Peels for Wound Healing.* Tissue Engineering and Regenerative Medicine, 2021. **18**(4): p. 561-571.
38. Zeng, L., et al., *Aloe derived nanovesicle as a functional carrier for indocyanine green encapsulation and phototherapy.* Journal of Nanobiotechnology, 2021. **439**.
39. Zhang, Y., Lan, M., Chen, Y., *Minimal Information for Studies of Extracellular Vesicles (MISEV): Ten-Year Evolution (2014–2023).* Pharmaceutics, 2024. **16**(11): p. 1394.
40. Sun, Z., Zheng, Y., Wang, T., Zhang, J., Li, J., Wu, Z., Zhang, F., Gao, T., Yu, L., Xu, X., Qian, H., Tan, Y., *Aloe Vera Gel and Rind-Derived Nanoparticles Mitigate Skin Photoaging via Activation of Nrf2/ARE Pathway.* International Journal of Nanomedicine, 2025. **20**: p. 4051-4067.
41. Syromiatnikova, V., Prokopeva, A., Gomzikova, M., *Methods of the Large-Scale Production of Extracellular Vesicles.* International Journal of Molecular Sciences, 2022. **23**(18): p. 10522.

42. Yang, Y., Wu, J., Xia, J., Wan, Y., Xu, J., Zhang, L., Liu, D., Chen, L., Tang, F., Ao, H., Peng, C., *Can aloin develop to medicines or healthcare products?* Biomedicine & Pharmacotherapy, 2022. **153**: p. 113421.
43. He, Y., Xi, J., Fang, J., Zhang, B., Cai, W., *Aloe-emodin alleviates doxorubicin-induced cardiotoxicity via inhibition of ferroptosis.* Free Radical Biology and Medicine, 2023. **206**: p. 13-21.
44. Salehi, B., Albayrak, S., Antolak, H., Kręgiel, D., Pawlikowska, E., Sharifi-Rad, M., Uprety, Y., Fokou, P., Yousef, Z., Zakaria, Z., Varoni, E., Sharopov, F., Martins, N., Iriti, M., Sharifi-Rad, J., *Aloe Genus Plants: From Farm to Food Applications and Phytopharmacotherapy.* International Journal of Molecular Sciences, 2018. **19**(9): p. 2843.
45. Bingqin, M., Weiyun, Q., Zhenguo, L., Liangzhi, W., *Effect of barbaloin on the NOX4/ROS/p38 MAPK signaling pathway and podocyte function in rats with diabetic nephropathy.* Chinese Journal of Comparative Medicine, 2020. **30**(9): p. 1-7.
46. Kumar, M., Sharma, S., Kumar, J., Barik, S., Mazumder, S., *Mitochondrial electron transport chain in macrophage reprogramming: Potential role in antibacterial immune response.* Current Research in Immunology, 2024. **5**: p. 100077.
47. Pérez, S., Rius-Pérez, S., *Macrophage Polarization and Reprogramming in Acute Inflammation: A Redox Perspective.* Antioxidants, 2022. **11**(7): p. 1394.
48. Viola, A., Munari, F., Sánchez-Rodríguez, R., Scolaro, T., Castegna, A., *The Metabolic Signature of Macrophage Responses.* Frontiers in Immunology, 2019. **10**.
49. Orihuela, R., McPherson, C., Harry, G., *Microglial M1/M2 polarization and metabolic states.* British Journal of Pharmacology, 2015. **173**(4): p. 649-665.
50. Lavogina, D., Lust, H., Tahk, M-J., Laasfeld, T., Vellama, H., Nasirova, N., Vardja, M., Eskla, K-L., Salumets, A., Rinken, A., Jaal, J., *Revisiting the Resazurin-Based Sensing of Cellular Viability: Widening the Application Horizon.* Biosensors, 2022. **12**(4): p. 196.
51. Riendeau, C., Kornfeld, H., *THP-1 Cell Apoptosis in Response to Mycobacterial Infection.* Infection and Immunity, 2003. **71**(1): p. 254-259.
52. Korns, D., Frasch, S., Fernandez-Boyanapalli, R., Henson, P., Bratton, D., *Modulation of macrophage efferocytosis in inflammation.* 2011. **2**.
53. Wang, S., Liang, Y., Dai, C., *Metabolic Regulation of Fibroblast Activation and Proliferation during Organ Fibrosis.* Kidney Diseases, 2022. **8**(2): p. 115-125.
54. Bernard, K., Logsdon, N., Ravi, S., Xie, N., Persons, B.., Rangarajan, S., Zmijewski, J., Mitra, K., Liu, G., Darley-Usmar, V., Thannickal, V., *Metabolic Reprogramming Is Required for Myofibroblast Contractility and Differentiation.* Journal of Biological Chemistry, 2015. **290**(42): p. 25427-25438.
55. Wang, F., Liu, J., An, Q., Wang, Y., Yang, Y., Huo, T., Yang, S., Ju, R., Quan, Q., *Aloe Extracts Inhibit Skin Inflammatory Responses by Regulating NF-κB, ERK, and JNK Signaling Pathways in an LPS-Induced RAW264.7 Macrophages Model.* Clinical, Cosmetic and Investigational Dermatology, 2023. **16**: p. 267-278.
56. Yadav, J., Verma, A., Pathak, P., Dwivedi, A., Singh, A., Kumar, P., Khalilullah, H., Jaremko, M., Emwas, A-H., Patel, D., *Phytoconstituents as modulators of NF-κB signalling: Investigating therapeutic potential for diabetic wound healing.* Biomedicine & Pharmacotherapy, 2024. **177**: p. 117058.
57. Eskandani, R., Kazempour, M., Farahzadi, R., Sanaat, Z., Eskandani, M., Adibkia, K., Vandghanooni, S., Mokhtarzadeh, A., *Engineered nanoparticles as emerging gene/drug delivery systems targeting the nuclear factor-κB protein and related signaling pathways in cancer.* Biomedicine & Pharmacotherapy, 2022. **156**: p. 113932.

58. Svitina, H., Hamman, J., Gouws, C., *Molecular mechanisms and associated cell signalling pathways underlying the anticancer properties of phytochemical compounds from Aloe species (Review).* Experimental and Therapeutic Medicine, 2021. **22**(2): p. 852.
59. Sapan, H., Paturusi, I., Jusuf, I., Patellongi, I., Massi, M., Pusponegoro, A., Arief, S., Labeda, I., Islam, A., Rendy, L., Hatta, M., *Pattern of cytokine (IL-6 and IL-10) level as inflammation and anti-inflammation mediator of multiple organ dysfunction syndrome (MODS) in polytrauma.* International Journal of Burns and Trauma, 2016. **6**(2): p. 37-43.
60. Luckett-Chastain, L., Calhoun, K., Schartz, T., Gallucci, R., *IL-6 influences the balance between M1 and M2 macrophages in a mouse model of irritant contact dermatitis.* The Journal of Immunology, 2016. **196**(1).
61. Niemand, C., Nimmesgern, A., Haan, S., Fischer, P., Schaper, F., Rossaint, R., Heinrich, P., Müller-Newen, G., *Activation of STAT3 by IL-6 and IL-10 in Primary Human Macrophages Is Differentially Modulated by Suppressor of Cytokine Signaling 3.* The Journal of Immunology, 2003. **170**(6): p. 3263–3272.
62. Fu, X.-L., Duan, W., Su, C-Y., Mao, F-Y., Lv, Y-P., Teng, Y-S., Yu, P-W., Zhuang, Y., Zhao, Y-L., *Interleukin 6 induces M2 macrophage differentiation by STAT3 activation that correlates with gastric cancer progression.* Cancer Immunoly, Immunotherapy, 2017. **12**: p. 1597–1608.
63. Gordon, S., Martinez, F., *Alternative Activation of Macrophages: Mechanism and Functions.* Immunity, 2010. **32**(5): p. 593-604.
64. Wu, W.-J., Wang, S-H., Wu, C-C., Su, Y-A., Chiang, C-Y., Lai, C-H., Wang, T-H., Cheng, T-L., Kuo, J-Y., Hsu, T-C., Lin, T-H., Lee, Y-J., *IL-4 and IL-13 Promote Proliferation of Mammary Epithelial Cells through STAT6 and IRS-1.* International Journal of Molecular Sciences, 2021. **22**(21): p. 12008.
65. Iwaszko, M., Biały, S., Bogunia-Kubik, K., *Significance of Interleukin (IL)-4 and IL-13 in Inflammatory Arthritis.* Cells, 2021. **10**(11): p. 3000.
66. Jiang, Y., Cai, R., Huang, Y., Zhu, L., Xiao, L., Wang, C., Wang, L., *Macrophages in organ fibrosis: from pathogenesis to therapeutic targets.* Cell Death Discovery, 2024. **10**(487).
67. Wynn, T., Vannella, K., *Macrophages in tissue repair, regeneration, and fibrosis.* Immunity, 2016. **44**(3): p. 450–462.
68. Kim, K., Sheppard, D., Chapman, H., *TGF-β1 Signaling and Tissue Fibrosis.* Cold Spring Harbor Perspectives in Biology, 2018. **10**(4): p. a022293.
69. Dikici, S., *Ascorbic Acid Enhances the Metabolic Activity, Growth and Collagen Production of Human Dermal Fibroblasts Growing in Three-dimensional (3D) Culture.* Journal of Science, 2023. **36**(4): p. 1625-1637.
70. Li, H., Yang, L., Zhang, Y., Gao, Z., *Kaempferol inhibits fibroblast collagen synthesis, proliferation and activation in hypertrophic scar via targeting TGF-β receptor type I.* Biomedicine & Pharmacotherapy, 2016. **83**(8): p. 967-974.
71. Jo, E., Park, S., Choi, Y., Jeon, W-K., Kim, B-C., *Kaempferol Suppresses Transforming Growth Factor-β1–Induced Epithelial-to-Mesenchymal Transition and Migration of A549 Lung Cancer Cells by Inhibiting Akt1-Mediated Phosphorylation of Smad3 at Threonine-179.* Neoplasia, 2015. **17**(7): p. 525-537.
72. Dou, F., Liu, Y., Liu, L., Wang, J., Sun, T., Mu, F., Guo, Q., Guo, C., Jia, N., Liu, W., Yi, D., Wen, A., *Aloe-Emodin Ameliorates Renal Fibrosis Via Inhibiting PI3K/Akt/mTOR Signaling Pathway In Vivo and In Vitro.* Rejuvenation Research, 2018. **22**(3).
73. Liu, H.Y., C., Wu, X., Peng, S., Zhou, L., McClements, D., Liu, W., *Influence of the maturity on the characteristics of orange-derived extracellular vesicles and their delivery performance for curcumin.* Food Chemistry, 2025. **485**: p. 144518.
74. Eliades, A. *Deep Green Permaculture*. 2019 [cited 2025 05/05]; Available from: https://deepgreenpermaculture.com/2019/04/16/identifying-and-growing-edible-aloe-

vera/#:~:text=A%20more%20definite%20way%20to,vera%20barbadensis%20Miller%20behind%20it.
75. Hęś, M., Dziedzic, K., Górecka, D., Jędrusek-Golińska, A., Gujska, E., *Aloe vera (L.) Webb.: Natural Sources of Antioxidants – A Review.* 2019. **74**: p. 255-265.
76. Martínez-Sánchez, A., López-Cañavate, M., Guirao-Martínez, J., Roca, M., Aguayo, E., *Aloe vera Flowers, a Byproduct with Great Potential and Wide Application, Depending on Maturity Stage.* Food, 2020. **9**(11): p. 1542.
77. Mensah, E., Adadi, P., Asase, R., Kelvin, O., Mozhdehi, F., Amoah, I., Agyei, D., *Aloe vera and its byproducts as sources of valuable bioactive compounds: Extraction, biological activities, and applications in various food industries.* PharmaNutrition, 2025. **31**: p. 100436.
78. Sonam, S., Tiwari, A., *Phytochemical Evaluation of Different Aloe Species.* International Journal of Chemical and Pharmaceutical Analysis, 2016. **3**(4).
79. Kumar, S., Yadav, A., Yadav, M., Yadav, J., *Effect of climate change on phytochemical diversity, total phenolic content and in vitro antioxidant activity of Aloe vera (L.) Burm.f.* BMC Research Notes, 2017. **10**(60).